A 3-D Shear Wave Velocity Model for Myanmar Region

Xin Wang[1] (ID), Shengji Wei[1,2], Yu Wang[1,3], Phyo Maung Maung[1], Judith Hubbard[1,2] (ID), Paramesh Banerjee[1], Bor-Shouh Huang[4] (ID), Kyaw Moe Oo[5], Thomas Bodin[6] (ID), Anna Foster[7] (ID), and Rafael Almeida[7] (ID)

[1]Earth Observatory of Singapore, Nanyang Technological University, Singapore, Singapore, [2]Asian School of the Environment, Nanyang Technological University, Singapore, Singapore, [3]Department of Geosciences, National Taiwan University, Taipei, Taiwan, [4]Institute of Earth Sciences, Academia Sinica, Taipei, Taiwan, [5]Department of Meteorology and Hydrology, Yangon, Myanmar, [6]Laboratoire de Géologie de Lyon: Terre, Planète, Environnemen, Université Lyon 1, CNRS, Villeurbanne, France, [7]School of Earth Science Energy and Environment, Yachay Tech University, Urcuquí, Ecuador

Abstract Myanmar is located at the eastern margin of the ongoing Indo-Eurasian collision system, has experienced a complex tectonic history and is threatened by a high level of seismic hazard. Here we develop a crustal scale 3-D seismic velocity model of Myanmar, which is not only critical for understanding the regional tectonic setting and its evolution but can also provide the foundation for a variety of seismological studies, including earthquake location determinations, earthquake focal mechanism inversions, and ground motion simulations. We use the newly deployed Earth Observatory of Singapore-Myanmar broadband seismic network and other seismic stations in and around Myanmar to study the station-based 1-D velocity structure through a joint inversion of receiver functions, H/V amplitude ratio of Rayleigh waves, and surface wave dispersion measurements. Our results reveal a highly variable crustal structure across Myanmar region, characterized by a series of N-S trending sedimentary basins, with thicknesses up to ~15 km in central Myanmar and an ~5-km step in the depth of the Moho across the Sagaing-Shan Scarp fault system. We interpolate our station-based 1-D velocity profiles to obtain an integrated 3-D velocity model from southern Bangladesh to Myanmar. Using three regional earthquakes located to the south, within, and north of the seismic network, we show that our proposed model performs systematically better than the CRUST 1.0 model for both Pnl waves and surface waves. Our study provides a preliminary community velocity model for the region, with further refinements and interpretations anticipated in the near future.

1. Introduction

The country of Myanmar, situated to the east of the Indian plate, on the southwestern margin of the Eurasian plate, occupies an important geologic position to understand the tectonic evolution of the Indo-Eurasia collision system (Figure 1; Gardiner et al., 2016; Ridd & Racey, 2015; Sloan et al., 2017; Wang et al., 2014). Myanmar is also a country threatened by a high level of seismic hazards with both its economic center (Yangon) and political capital (NayPyiTaw) located on or near the active Sagaing fault (Hurukawa & Maung Maung, 2011; Wang et al., 2011, 2014; Xiong et al., 2017). Thus, a better understanding of the crustal-scale velocity structure of Myanmar could have a major impact in unraveling the regional tectonics, improving the quality of seismological studies (e.g., earthquake hypocenter determinations, focal mechanism inversions, and ground motion simulations), and potentially help to mitigate the seismic hazard and risk in this area.

The present-day tectonics of Myanmar are a result of the collision between the Indian and the Eurasian plates, which began approximately 50 Ma ago (Gardiner et al., 2016; Sloan et al., 2017; Socquet et al., 2006). The entire region is mainly composed by a series of elongate, north-south-oriented tectonic blocks, including the Indo-Burman Ranges (IBR), the Central Myanmar Basin (CMB), and the Shan-Thai Block (STB; Figure 1). The IBR, extending from northeast India and eastern Bangladesh to western Myanmar, has been interpreted as an accretionary prism consisting primarily of Cretaceous to Eocene sediments with Mesozoic ophiolites associated to the subducted Indian Ocean lithosphere (Maurin & Rangin, 2009). The CMB lies between the IBR to the west and the Sagaing fault to the east and is composed of a series of fore-arc or back-arc Cenozoic sedimentary basins with sparsely distributed volcanic bodies (Pivnik et al., 1998). Further east, the STB, extending from eastern Myanmar to southern China and northern Thailand, is composed of Cambrian to Triassic sedimentary rocks and Precambrian high-grade metamorphic rocks
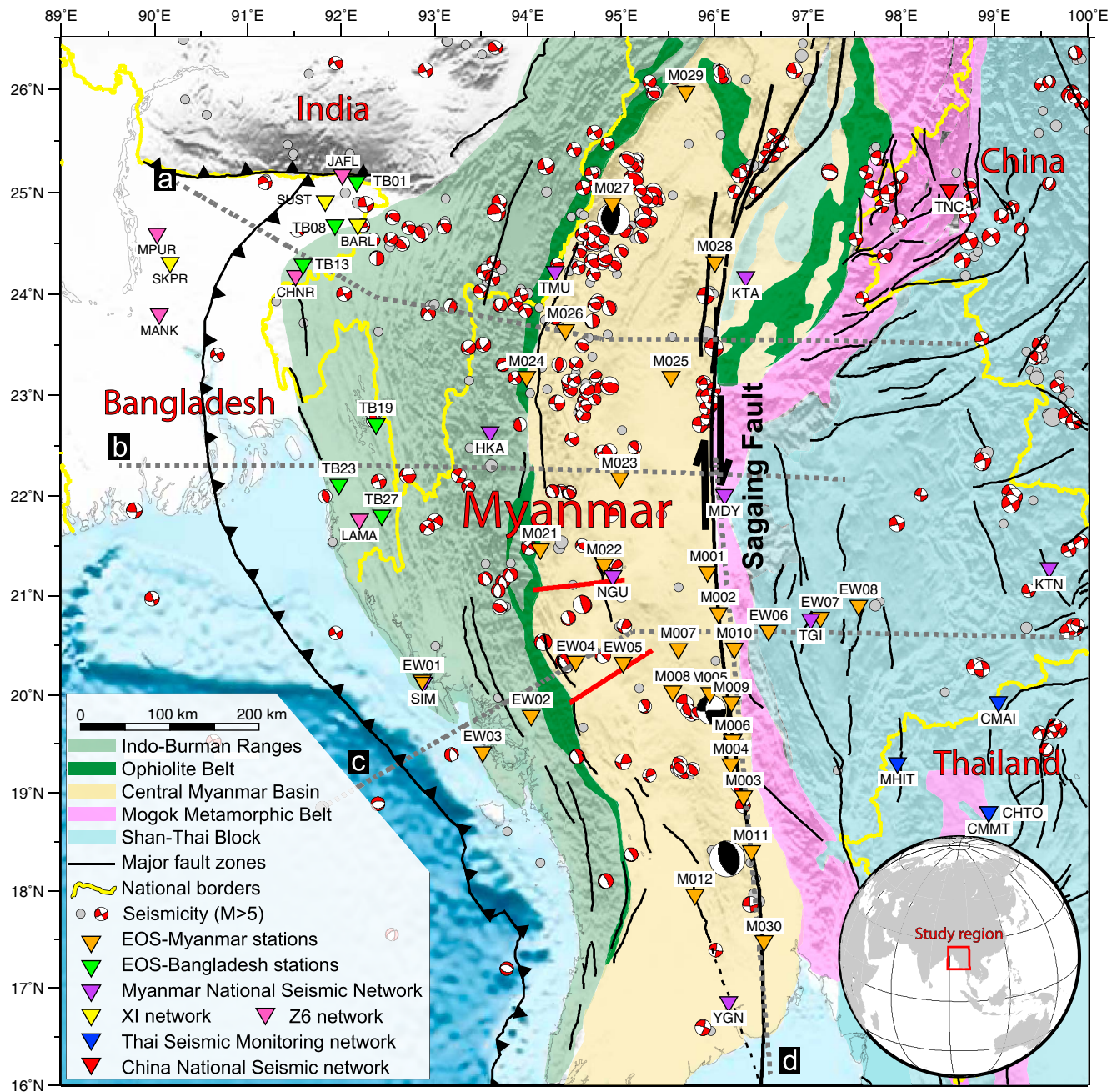
Figure 1. Overview map of the study region, showing simplified geological units (modified from Searle et al., 2017), major faults (modified from Wang et al., 2014) and seismicity (magnitude larger than 5.0 from the EHB [Engdahl et al., 1998] and GCMT [Ekstrom et al., 2012] catalogues from 1980 to 2018). The colored triangles show the seismic stations used in this study. The dotted gray lines and red lines indicate the locations of profiles shown in Figures 7 and 10, respectively. The black beach balls in northern, central, and southern Myanmar show the locations and focal mechanisms of three earthquakes used in the 3-D waveform simulations in section 7.3.

(Gardiner et al., 2016; Searle et al., 2007). These diverse geologic settings result in strong seismic-velocity heterogeneities in the lithosphere along the eastern margin of the Indian-Eurasian collision system (Bao et al., 2015; Yao et al., 2010). Mapping the seismic velocities of these different blocks can thus help us understand the regional tectonics and geology, as well as their evolution.

In addition to the strong seismic-velocity heterogeneities, significant seismicity has also been recorded in the Myanmar region. The bulk of the seismicity that occurs in Myanmar corresponds to the Burma subduction

zone, with maximum earthquake depths of ~160 km (Hurukawa et al., 2012; Ni et al., 1989; Stork et al., 2008). The Sagaing fault, a dextral strike-slip fault running from the Eastern Himalayan Syntaxis in the north, to the Andaman Sea in the south, has produced more than six M7.0+ earthquakes in the last century, leaving a 200-km-long seismic gap between Myanmar's new capital NayPyiTaw and its second largest city Mandalay (Hurukawa & Maung Maung, 2011). In addition, many crustal earthquakes have occurred within the Burma plate, indicating distributed deformation within the crust (Figure 1; Hurukawa et al., 2012; Wang et al., 2014). The high seismicity levels, potential for large earthquakes, and anticipated amplification caused by sedimentary basins (e.g., CMB), result in a high level of seismic hazard in this region. As a consequence, a reliable crustal-scale velocity model of Myanmar is essential for accurate and precise studies of many seismological topics, to mitigate the seismic hazard and risk in the region.

Despite the complex geologic setting and the high level of seismic hazards of this area, the regional-scale seismic velocity structure beneath Myanmar remains enigmatic, mainly due to the lack of local and regional seismic waveform observations (Thiam et al., 2017). Former investigations on the velocity structure beneath Myanmar were primarily made using teleseismic analyses, with global-scale resolution (Li et al., 2008; Obayashi et al., 2013; Pesicek et al., 2010). These studies have revealed the first-order geometry and velocity anomaly of the downgoing slab in the Burma subduction zone at a resolution of ~200 km at best and thus do not provide any constraints on the velocity structure of the overriding lithosphere (e.g., the Burma Plate). On the other hand, localized studies of the structure of the upper crust have been conducted mainly for petroleum exploration purposes (e.g., Pivnik et al., 1998; Ridd & Racey, 2015). For example, by using seismic reflection profiles combined with regional stratigraphic and field-based geological observations, Pivnik et al. (1998) suggested that the sediment thickness of CMB reaches as thick as 18 km. Those seismic reflection studies, however, have only been conducted in a few places with limited depth penetration. Furthermore, integrated crustal-scale 3-D velocity models of Myanmar are only available from global databases, such as the CRUST 1.0 model (Laske et al., 2013), in which the crustal structure beneath Myanmar was mainly constrained by the regional tectonic setting, gravity data, and statistical averages of crustal properties. The accuracy of this global model has not yet been verified due to the lack of regional seismic waveform observations.

In this study, we make use of the newly deployed Earth Observatory of Singapore-Myanmar (EOS-Myanmar) seismic network and other available seismic stations in and around Myanmar to constrain the regional crustal-scale seismic velocity structure. In the following sections, we first give an overview of our newly installed EOS-Myanmar seismic network. We then obtain a station-based 1-D velocity model beneath each station using a joint inversion of receiver functions (RFs), H/V amplitude ratio of Rayleigh waves (H/V ratio), and surface wave dispersion (SWD) measurements. We interpolate our station-based 1-D velocity profiles to obtain an integrated 3-D velocity model from southern Bangladesh to Myanmar. We compare our results with other independent geological and geophysical investigations and discuss similarities and discrepancies. To further verify our velocity model, we use three regional earthquakes located to the south, interior, and north of the seismic array to calculate 3-D waveform synthetics and compare the performance of our model with that of the CRUST 1.0 model in a systematic way. This is followed by a discussion and conclusions.

2. Seismic Station Configuration and Sensor Misorientation

In our study, we use seismic data collected from 56 regional broadband stations in and around Myanmar, including 34 stations operated by the EOS and 22 stations downloaded from the Incorporated Research Institutions for Seismology (IRIS) database (Figure 1 and Table S1).

About half of our data is collected from the EOS-Myanmar seismic network, which comprises 28 broadband stations, distributed throughout Myanmar with linear concentrations along and perpendicular to the Sagaing fault in the middle of the country (Figure 1). The EOS-Myanmar seismic network deployment was started in January 2017, and all of these stations were installed and transmitting data in real time by July 2017. In addition to the EOS-Myanmar seismic network, we include six temporary broadband stations deployed in Bangladesh as part of the TREMBLE network (Temporary Receivers for Monitoring BangLadesh Earthquakes), operated by EOS in conjunction with Dhaka University. Three of these stations have been in operation since June 2016, and the other three were deployed in September or October of 2016.

In this study, we analyzed waveform data recorded by the EOS-Myanmar network between July 2017 and April 2018 and by the TREMBLE network between June 2016 and December 2017. To improve the spatial coverage of the region, we also include 22 IRIS broadband stations (station name and operation period can be found in Table S1 in the supporting information) in and around Myanmar. Some of these stations have been used in previous studies to obtain 1-D velocity structures beneath the stations (Bai et al., 2010; Hu et al., 2008; Mitra et al., 2018; Noisagool et al., 2016; Singh et al., 2016); we compare these with our results for verification and discussion (see section 7.1). As shown in Figure 1, the average station spacing (~150 km) is too coarse to apply modern array processing techniques, such as crustal-scale RF common-conversion-point stacking (Zhu, 2000). Therefore, we focus on resolving the 1-D velocity structure beneath each station by a joint inversion of RF, H/V ratio, and SWD measurements.

Before the joint inversion, we inspect and correct the sensor misorientation using the P wave particle motion method (Niu & Li, 2011; Wang et al., 2016), because both RF and H/V ratio of Rayleigh wave studies strongly depend on accurate orientations of the horizontal components. We collect the horizontal waveform data from teleseismic earthquakes then apply a single-earthquake principal component analysis (PCA), as well as the multiearthquakes minimizing transverse energy ($_{min}$T) method to the long-period (5–50 s) teleseismic P waveforms to estimate the sensor orientations (Figures 2a–2c; see Wang et al., 2016, for more details on the method). During the early stage of the deployment (July 2017 to April 2018), we found that about one third of our stations had sensor misorientations greater than 10° (Figure S1 and Table S2). To verify our results, we use the Rayleigh wave particle motion to check if the corrected sensor orientations improve the cross-correlation coefficients (CCCs) between the vertical and phase-delayed radial components of Rayleigh waves at long periods (25–50 s). If there is no sensor misorientation, the CCC is expected to be close to 1 in an isotropic medium (Rueda & Mezcua, 2015). We obtain a significant improvement of the CCC after correcting the sensor misorientation (Figure 2d), indicating a robust result from our analysis. The sensor misorientation results for all of the EOS-Myanmar stations are given in Table S2.

3. Data Analysis

In recent years, it has become common to jointly invert RF waveforms, H/V ratio, and SWD measurements to image subsurface velocity structures (Bodin et al., 2012; Chong et al., 2016; Lin et al., 2012; Shen et al., 2012; Shen & Ritzwoller, 2016). The RF waveforms are particularly powerful for capturing sharp velocity contrasts between neighboring layers beneath a station, while the SWD and H/V ratio are more sensitive to the absolute velocity structure over a certain range of depths. A joint inversion of these complementary data sets can reduce uncertainties and produce more reliable velocity models. In this study, we use a trans-dimensional Markov chain Monte Carlo (McMC) Bayesian approach (Bodin et al., 2012) to simultaneously invert RFs, H/V ratio, and SWD measurements to obtain a crustal-scale 1-D velocity model below each station.

3.1. Receiver Function Data Processing

The P wave RFs are time series obtained by deconvolving the vertical component from the radial component of teleseismic P waves, which contains the arrival time and amplitude information of converted phases produced by velocity interfaces beneath a seismic station (Langston, 1979). Stacking RFs from a large number of teleseismic events improves the signal-to-noise ratio (SNR) of the converted phases (e.g., P-to-s) and their multiples. Inverting the stacked RF waveforms can therefore provide constraints on the velocity structure beneath the stations.

We collect waveform data from teleseismic events with M > 5.2 and epicentral distance ranges of 30° to 90° for the P wave RF study. We window raw data between 20 s before and 100 s after the first P arrival and rotate the horizontal components to the radial and transverse components. The three-component seismograms are then zero-phase filtered to 50 s to 2 Hz to eliminate both long-period and high-frequency noise. We obtain radial RFs by using a time-domain iterative deconvolution technique with a Gaussian low-pass filter (Gaussian parameter of 1.5, central frequency around 0.75 Hz; Ligorría & Ammon, 1999). We then normalize the radial RF by the maximum amplitude of the vertical RF, which is obtained by deconvolving the vertical component by itself, to obtain the true RF amplitude (Ammon, 1991). We discard those RFs that have large coda amplitude after the first P arrival (e.g., >20% of the direct P wave amplitude). We then visually inspect the results to remove bad RFs for which the waveforms are not coherent with each other. The
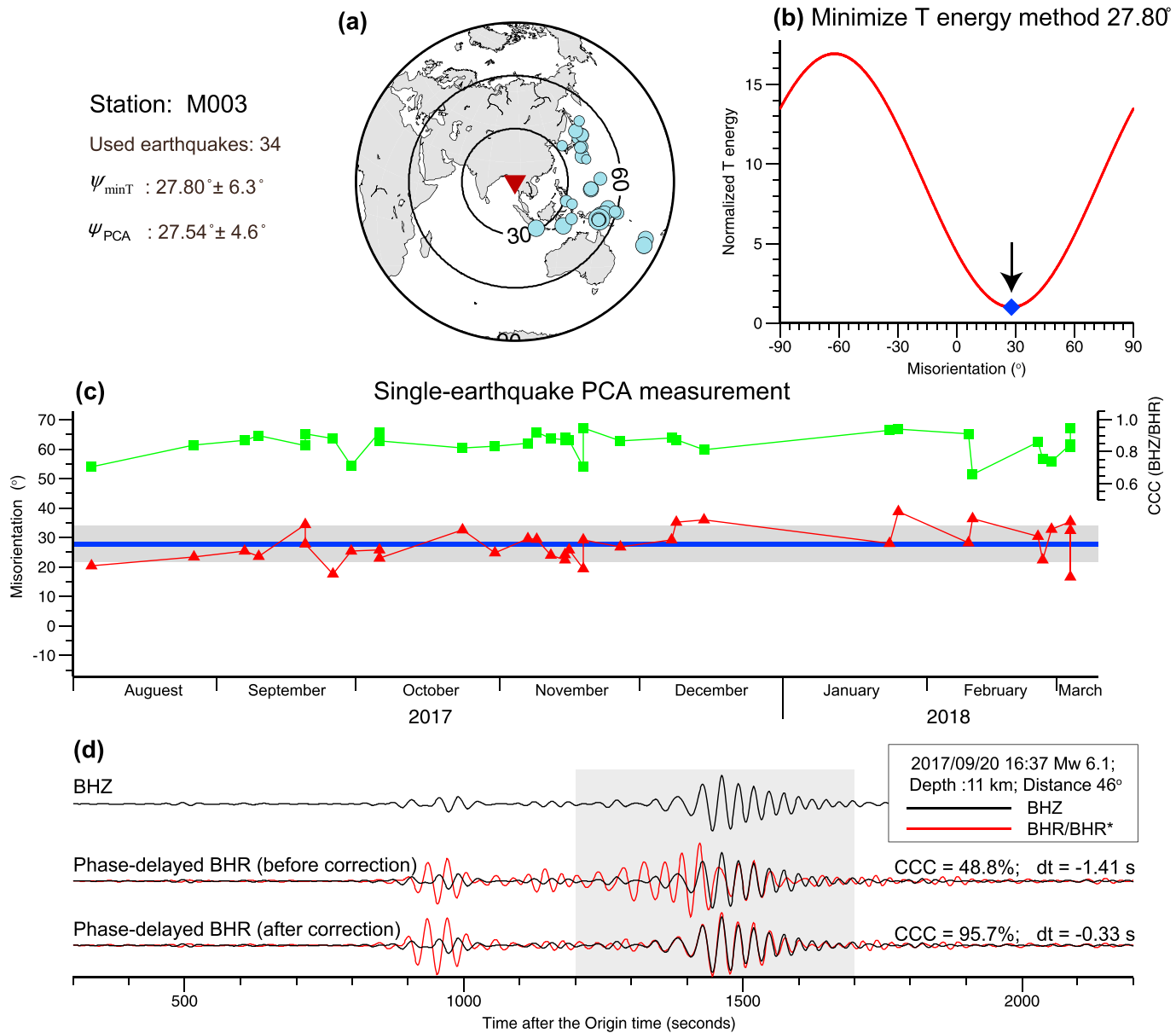
Figure 2. An example showing the detection and correction of sensor misorientation for station M003. The upper-left text indicates the station name, number of earthquakes used, and results from the minimizing transverse energy method and principal component analysis (PCA) method (Wang et al., 2016). (a) Earthquake distribution used in this analysis. (b) For a suite of events, the misorientation angle is determined by minimizing the summed energy of the transverse component. (c) Results from single-earthquake PCA. The red triangles indicate single-earthquake measurements sorted by date. The corresponding green squares in the upper panel are the cross-correlation coefficients (CCCs) between the vertical and radial P waves, which serves as proxies of the waveform quality. The blue line shows the average misorientation value. (d) Long-period (25–50 s) Rayleigh wave records on vertical (black) and phase-delayed radial components (red) from an Mw 6.1 earthquake. Note the improvement in the waveform match before and after the sensor misorientation was corrected.

final RF data set consists of 12,794 high-quality waveforms, with the number of RFs for each station varying due to different site conditions and operation periods. On average, each EOS-Myanmar station has approximately 130 RFs.

Most of the RFs are obtained from earthquakes located to the northeast and southeast of the array (Figures 3a and 3d). For some of the stations, for example, EW04 and EW07 in Figure 3b, the RF waveforms from different back azimuths show distinct differences, likely related to dipping structure and/or crustal-scale anisotropy beneath the stations (Long, 2013). In addition, the amplitudes of the direct P phase clearly show an epicentral dependence (Figure 3f), which can be largely explained by the move-out effect due to
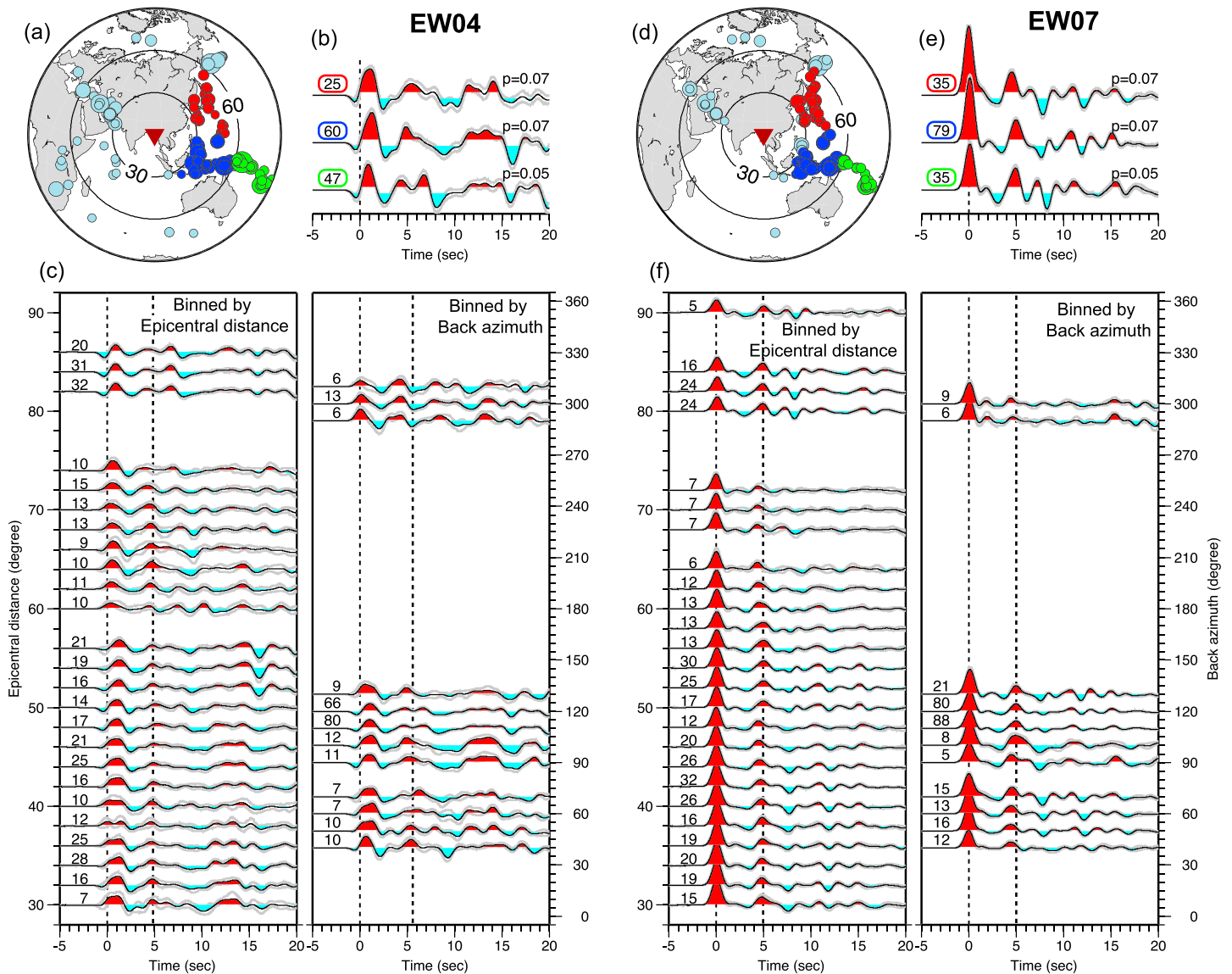
Figure 3. Examples illustrating the receiver function (RF) data processing for stations EW04 (a–c) and EW07 (d–f). (a) The earthquake distribution, where the red, blue, and green dots indicate the three bins used to group the RFs. (b) The stacked RFs (solid lines) bounded by 95% confidence levels (gray lines) estimated by the bootstrapping method. The number of earthquakes used in stacking is shown at the start of the waveform, corresponding to the number of dots in (a). The averaged ray parameter, p, is given at the end of each waveform. (c) All the RFs. For better illustration, the RF waveforms have been stacked by epicentral distance (15° bins with increment of 2°) and back azimuth (15° bins with increment of 10°). The number at the left indicates the number of stacked traces in each bin. (d–f) The results for station EW07. Note the azimuthal dependence of the Ps arrivals and amplitudes, and the distance dependence of the amplitude of the direct P signal.

different incident angles (Figure S2). Direct stacking RFs aligned on the direct *P* phase could result in smaller amplitudes of the following phase, especially for reverberations (Figure S2). In principle, this problem can be partially solved by narrowing the distance and azimuth range of the RFs used in stacking and inversion. Thus, in this study, we group the RFs into three bins: (1) distance 30–60° and back azimuth 30–90°, (2) distance 30–60° and back azimuth 90–150°, and (3) distance 60–90° and back azimuth 90–150° (Figures 3a and 3d), based on the fact that most of the earthquakes are distributed within these narrow azimuthal and distance ranges.

For each bin, we estimate the mean RF waveforms and corresponding uncertainties using a bootstrapping method (Efron & Tibshirani, 1991). In each bootstrapping session, we randomly select 90% of RF traces from the original database, allowing duplicates. We then estimate the stacked RF waveforms for each new data

set. The resulting stacked RF waveforms from all bootstrapping sessions are expected to be distributed around the true value. The mean amplitude of each sampling point (t) is then obtained as the average of the trials, $\overline{Amp(t)} = \left(\sum_{i=1}^{N} Amp(t)_i \right) / N$, where $Amp(t)_i$ is the amplitude of t's sampling point in the ith bootstrapping, and N is the number of bootstrapping trials ($N = 500$ in this study). The standard deviation of each sampling point is calculated using $\sigma(t) = \sqrt{\left(\sum_{i=1}^{N} \left(Amp(t)_i - \overline{Amp(t)} \right)^2 \right) / (N - 1)}$. The mean RF waveforms are then used as data and the estimated standard deviations are used as data error (see section 4) in the following joint inversion. To ensure reliability, we only use bins with more than 20 RFs for inversion. We invert three independent velocity models for each station based on the data from different back azimuths and distances. The final 1-D velocity profile for each station is the average of these three models. A detailed study of the complex 3-D structure (e.g., anisotropy and dipping layer) beneath each station will left for further investigations.

3.2. Measurement of H/V ratio

The H/V ratio, also called the Rayleigh wave ellipticity, is defined as the amplitude ratio between the radial and vertical components of Rayleigh waves measured at various frequencies. Similar to the RF, the H/V ratio is also a station-based measurement. It is particularly sensitive to the shallow velocity structure beneath the station (Li et al., 2016; Lin et al., 2012; Maupin, 2017; Tanimoto & Rivera, 2008).

We measure the H/V ratio at each station following the procedures proposed by Tanimoto and Rivera (2008). Here we briefly describe the key data processing steps. For each station, we collect waveforms for shallow (depth < 50 km) earthquakes that have magnitude greater than 5.5 and are located at epicentral distances between 20° and 120° (Figure 4a). We remove the instrument response, subtract the mean and linear trends of the seismograms, and decimate the sampling intervals to 1 s (Figure 4b). We then filter the radial and vertical components by a series of narrowband phase-matched Gaussian filters (Bensen et al., 2007), with the central frequency varying from 25 to 75 s. These frequency bands provide strong constraints on the velocity structure in the basin and the crust (Figure S3). We apply the Hilbert transformation to the radial component to correct the Rayleigh wave phase shift between the vertical and radial components, before calculating the CCC between them. The CCC serves as a proxy for quality control in the later steps (Tanimoto & Rivera, 2008). The H/V ratio at each frequency band is obtained by using the maximum amplitude of the envelopes of the vertical and radial components (Figure 4c).

To ensure reliable measurements, we only select data with an SNR greater than 8 in both vertical and radial components (Li et al., 2016; Lin et al., 2012). Here SNR is defined as the amplitude ratio between the surface wave and the average amplitude of the waveform 500 to 1,000 s after the Rayleigh wave. In addition, we only select measurements with CCC between the vertical and the phase-shifted radial components greater than 85% in order to minimize the impact of 3-D velocity structure and body waves (Tanimoto & Rivera, 2008). For each period, all of the H/V measurements satisfying the aforementioned criteria are used to obtain the average H/V ratio and the associated uncertainties, estimated using a bootstrapping method (Efron & Tibshirani, 1991). Figure 4 shows an example of an H/V measurement at station EW04. Figure S4 summarizes a subset of H/V ratio measurements for all of the stations at 30, 40, 50, and 60 s, where clear correlation between H/V ratios and surface geology is observed: high H/V ratios in basins and low H/V ratios in mountain ranges. These H/V ratio measurements are used in the joint inversion in a later step.

3.3. The Rayleigh Wave Phase Velocity Measurement

The above-mentioned RF and H/V ratio are station-based measurements and can be combined to constrain the velocity structure beneath a station in a joint inversion. However, Chong et al. (2016) showed that this kind of joint inversion only provides limited constraints on the absolute velocity. Complementary, Rayleigh wave phase velocity dispersion measurements are more sensitive to the absolute velocity. We therefore also include the phase velocity of Rayleigh waves in our joint inversion.

We measure the phase velocities of Rayleigh waves at various frequencies using the Automated Surface Wave Phase Velocity Measuring System proposed by Jin and Gaherty (2015). The Automated Surface Wave Phase Velocity Measuring System measures the phase delay between station pairs via cross correlation of fundamental mode surface waves from earthquakes (Jin & Gaherty, 2015). To apply this method to our
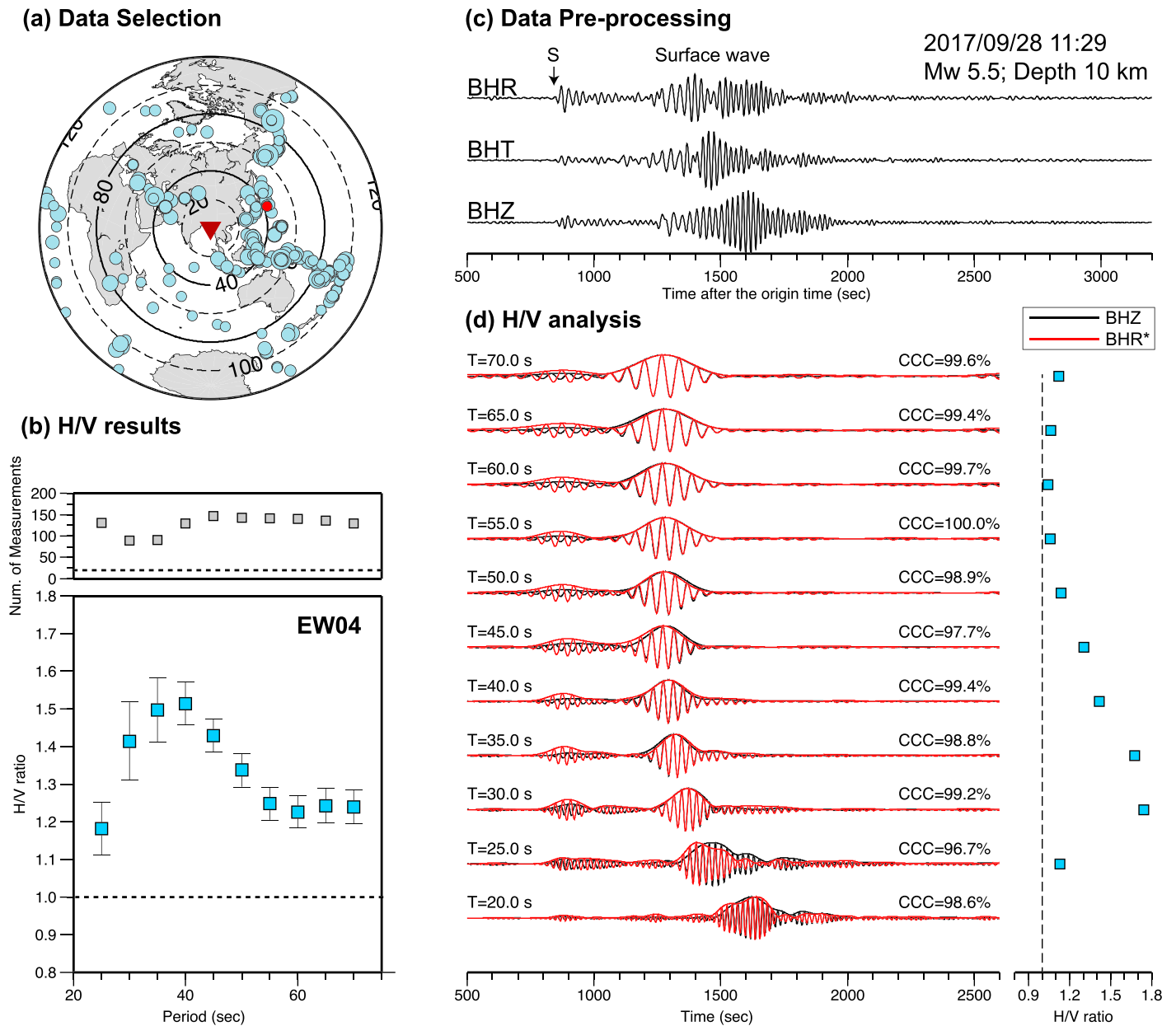
Figure 4. Example of data processing for the H/V amplitude ratio of Rayleigh waves. (a) The earthquakes used in this study, where the red dot indicates the sample earthquake shown in (c) and (d). (b) The measurements and associated uncertainties of H/V ratio obtained using all the earthquakes recorded by station EW04. The gray squares in the top panel indicate the number of earthquakes used for this station. (c) An example showing the long-period three-component seismic waveforms (filtered to 20–100 s). (d) An example showing the H/V ratio analysis. The black and red lines show the narrowband-filtered vertical and phase-delayed radial components. The waveforms have been aligned by cross correlation. The envelopes of the vertical and phase-delayed radial components are superimposed on the top. The right panel shows the H/V ratio measurements obtained using this earthquake.

data set, we collect waveform data for earthquakes that have epicentral distances ranging from 10° to 140°, with a magnitude greater than 5.5 and focal depth less than 50 km. The data processing includes two key steps. First, we obtain the phase delay for certain periods by cross-correlating the waveforms between two stations, noting that we only conduct measurements for station pairs with spacing less than 300 km to minimize cycle skipping (Jin & Gaherty, 2015). Second, we combine phase delays measured for different periods to invert for 2-D phase velocity maps using the Eikonal and Helmholtz tomography method (Lin et al., 2009; Lin & Ritzwoller, 2011; see Jin & Gaherty, 2015, for more details of the methodology). Following these procedures, we obtain phase velocity maps at a range of periods (30–80 s), as shown in
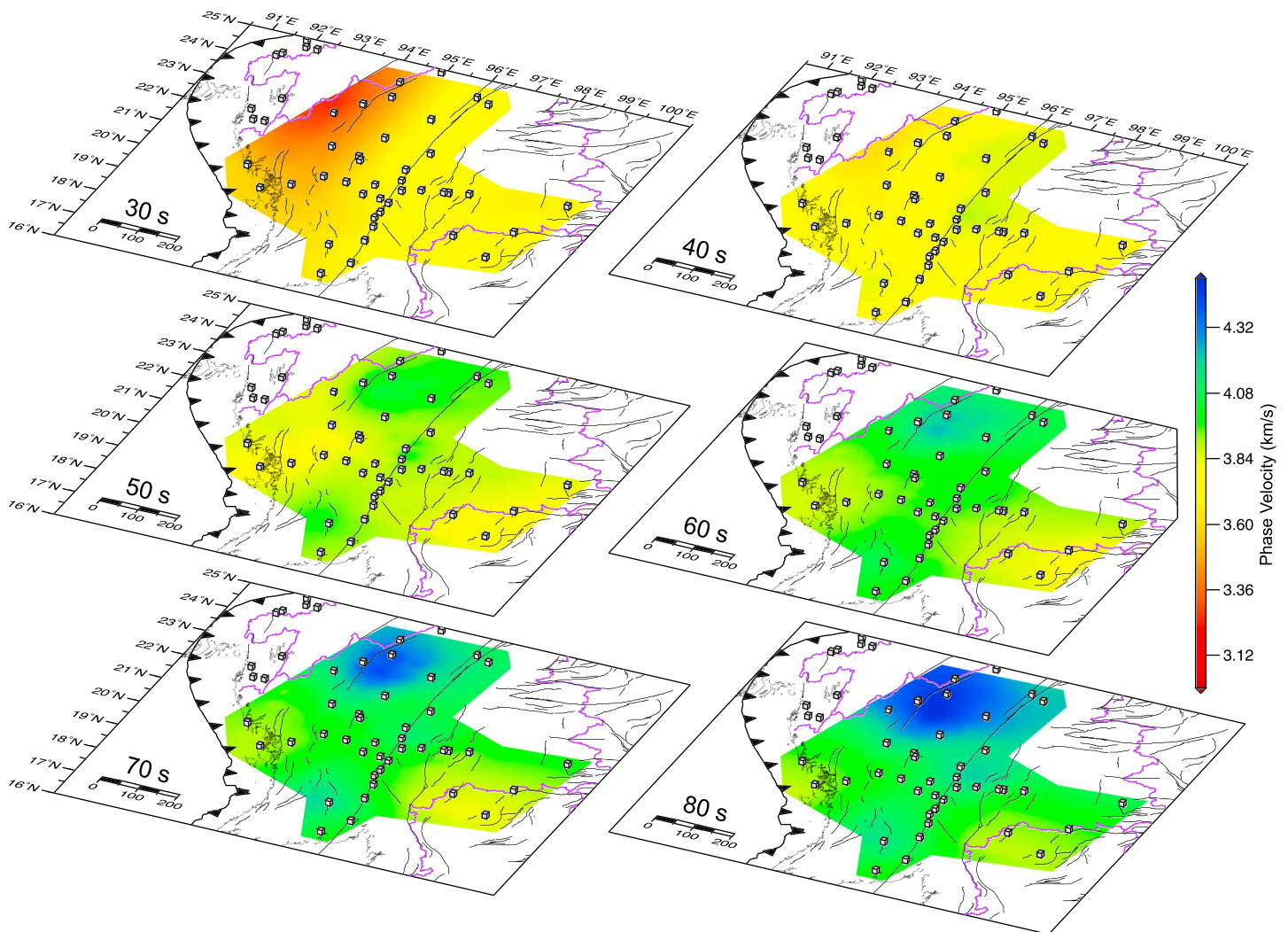
Figure 5. Phase velocity maps for different frequency bands derived from earthquake tomography. The period for each map is marked in the bottom-left corner of each panel. More details about the ray coverage, checkerboard tests, and associated uncertainties are given in the supporting information (Figures S5–S10).

Figure 5. The raypath coverage and checkerboard tests for different periods are presented in the supporting information (Figures S5–S8). Checkerboard tests indicate that our data set provides a general resolution of ~1.0° in the area, with ~0.5° spatial resolution in the center of the network. The shorter period in general has better resolution than longer period. Due to the limited station coverage, our phase velocity measurements show lower resolution in northern Myanmar and around the edge of the network than the rest of the area (Figures S9 and S10). We are not able to obtain a phase velocity map for Bangladesh and the IBR, as the observation time span of stations in these regions do not overlap with the rest of the network (Figure 1 and Table S1; e.g., the XI network was working from 2008 to 2010, the Z6 network was installed from 2011 to 2015, and the EOS TREMBLE network has been in operation from 2016 to present). An in-depth investigation of the surface wave tomography in the region is left for future studies; here we focus on retrieving 1-D SWD for each station from the Rayleigh wave phase velocity maps (Figure 5) and using them in a joint inversion.

4. Joint Inversion Through a Transdimensional Bayesian Approach

In this section, we show how the 1-D shear wave velocity model beneath each station is obtained by jointly inverting the RFs, H/V ratio, and SWD measurements through a transdimensional McMC Bayesian

approach (Agostinetti & Malinverno, 2010; Bodin et al., 2012; Dettmer et al., 2010; Green, 2003; Hopcroft et al., 2007; Luo, 2010; Malinverno, 2002; Minsley, 2011). In this work, we follow the procedure in Bodin et al. (2012) that was designed for joint inversion of RF and SWD and modify the code to also include the H/V ratio in the joint inversion.

In the Bayesian framework, the solution to the inverse problem is the posterior distribution $p(m \mid d)$ that represents the probability of the velocity model m, given the observed data d. Bayes theorem states that the posterior distribution is proportional to the likelihood distribution $p(d \mid m)$, multiplied by the prior probability distribution, $p(m)$. The likelihood function, $p(d \mid m)$, quantifies how well a given velocity model, m, can reproduce the observed data. The prior probability represents the level of information about the model m before measuring data. For more details about Bayesian inference, we refer the reader to Box and Tiao (2011). Below we show how the prior probability distributions and likelihood function are defined in our problem, and we sample the posterior probability distribution of the velocity model through a McMC approach.

4.1. Model Parameterization and Prior Probability Distributions

In the joint inversion, we use the RF waveform window defined as 5 s before to 15 s after the direct P waves, and the H/V ratio and SWD measured at 25–70 s and 30–80 s, respectively. The complementary nature of these data sets provides strong constraints on the velocity structure in the crust and uppermost mantle (Figure S3). Thus, we invert the 1-D velocity model beneath each station down to 100 km.

In our inversion, the 1-D velocity model is parameterized through a transdimensional approach, where the number of layers is considered as variable in the inversion (Bodin et al., 2012). The number of layers is given a wide prior uniform distribution, that is, it is allowed to vary between 1 and 50, even though this number in most of the inversions converges to 20–30. The thickness and shear wave speed of each layer are also variables. We assume a uniform prior distribution of shear wave velocity varying from 1.0 to 5.0 km/s, and the bottom layer is a half space with shear speed ranging from 4.0 to 5.0 km/s. With this setup, our model space has a large degree of freedom, allowing us to capture the shallow sedimentary structure and/or any low velocity zones within the crust. We conduct the inversion only for shear wave velocity, and the corresponding P wave velocity and density are obtained through empirical relations (Brocher, 2005).

4.2. The Likelihood Function and Posterior Probability Distributions

In the case of a joint inversion of different data types, and assuming errors for different data are independent, the likelihood function can be written as the product of the likelihoods for each data type, $p(d \mid m) = p(d_{RF} \mid m)p(d_{H/V} \mid m)p(d_{SWD} \mid m)$. Assuming data errors are independent and normally distributed, the likelihood function takes the form, $p(d_{\mathrm{obs}} \mid m) = \frac{1}{\sqrt{(2\pi)^n \mid C_e \mid}} \times \exp\left\{ \frac{-(d_{\mathrm{syn}} - d_{\mathrm{obs}})^T C_e^{-1}(d_{\mathrm{syn}} - d_{\mathrm{obs}})}{2} \right\}$, where n is the number of data points (sampling points in an RF time series or number of periods considered in H/V ratio and SWD measurements), d_{syn} are synthetic data predicted for model m, d_{obs} are the observations, and C_e is the data error covariance matrix (Bodin et al., 2012). We stress that the data errors for different data types directly control the relative weights between the RF, H/V ratio, and SWD in the joint inversion. In this work, we use a hierarchical Bayes formulation and also consider the errors in C_e as unknown in the inversion (Bodin et al., 2012; Malinverno & Briggs, 2004; Malinverno & Parker, 2006). The minimum allowable error is defined as 0, and the maximum allowable error is set to be twice the measured uncertainties obtained in section 3, as we acknowledge that the uncertainty estimation using the bootstrapping method may be underestimated. We also tested different maximum allowable errors and found that they do not affect the final results when the observations are well fitted. More details regarding the inversion algorithm can be found in Bodin et al. (2012).

We run the inversion on 400 CPU cores to simultaneously and independently sample the model space. On each CPU, a random walk in the model space is performed for 80,000 steps with the reversible jump McMC algorithm (Bodin et al., 2012; Green, 1995). The first 50,000 samples are discarded as burn-in steps. Then, we select one model out of 10 in the subsequent 30,000 steps as the ensemble solution. The solution of the problem is given by this ensemble of collected models, which approximates the posterior probability distribution. In terms of choosing a single velocity model for interpretation in the later section, we only focus on
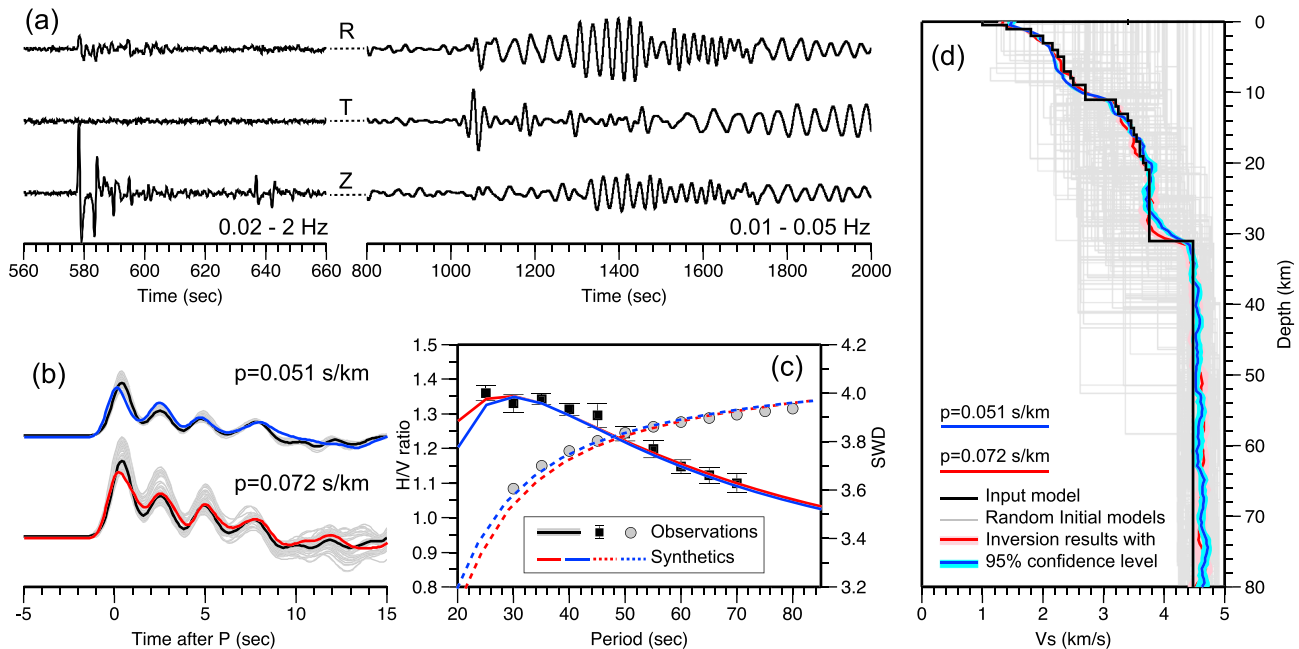
Figure 6. Synthetic tests for joint inversion. (a) Examples of synthetic seismograms with noise added. (b) Synthetic receiver function (RF) waves, where the gray lines show all the RF waveforms obtained using earthquakes from different distances. The RF waveforms have been grouped and stacked based on the epicentral distance range used in the real data, resulting in the stacked RF waveforms shown as black lines. The corresponding average ray parameter, p, is shown. The red and blue lines show synthetic RFs predicted by the mean velocity models shown in (d). (c) The H/V ratio and surface wave dispersion (SWD) fits, where the squares and circles indicates the H/V ratio and SWD measurement, respectively. The solid and dashed lines indicate the results from joint inversion. (d) The obtained posterior mean velocity models for the two inversions are shown in red and blue, and the input velocity model is shown in black for reference. We also show in gray lines the first 100 initial models of each independent Markov chain, generated randomly from the prior distribution.

the posterior mean velocity model beneath each station, which is obtained by averaging all the collected models.

4.3. Synthetic Tests

To test the inversion algorithm, we first apply it to synthetic data. We design an Earth model consisting of a thick sedimentary layer superimposed on the Preliminary Reference Earth Model (Dziewonski & Anderson, 1981). We then use a frequency-wave number method (Zhu & Rivera, 2002) to generate 1-D synthetic seismograms for distant earthquakes with numerical accuracy up to 5 Hz. The epicentral distance and azimuthal distribution of earthquakes roughly follow the real data (Figure 3a). Random Gaussian colored noise, with a natural frequency of 1 Hz, is added to mimic the noise in the real data (Figure 6a). We process the synthetic seismograms using the same procedures described in section 3 to get the synthetic RF and H/V ratio. We do not calculate SWD using the synthetic seismograms, as the SWD requires multistation cross correlation. Instead, we generate synthetic SWD measurements by normal mode summation using the DISPER80 package developed by (Saito, 1988). Figures 6a–6c show the synthetic seismograms with noise and the obtained RF waveforms, H/V ratio, and SWD. A delayed first P arrival and large H/V ratio suggest the influence of a sedimentary layer (Yeck et al., 2013). Figure 6d shows the inverted posterior mean velocity models together with the 95% confidence level. The fits for RF waveforms, H/V ratio, and SWD predicted from the mean model are shown in Figures 6b and 6c, respectively. Our synthetic test shows that we can recover the input model relatively well (Figure 6d), including the sharp Moho and a shallow sedimentary layer. We acknowledge that real data have much more complex waveforms than the synthetics given here; for example, we do not consider anisotropy or 2-D/3-D structural effects in our synthetic tests. To further verify the inversion results for the real data, we compare our results with previous studies and use 3-D waveform simulations to quantify the performance of our velocity model against CRUST 1.0 model. These are detailed in section 8.

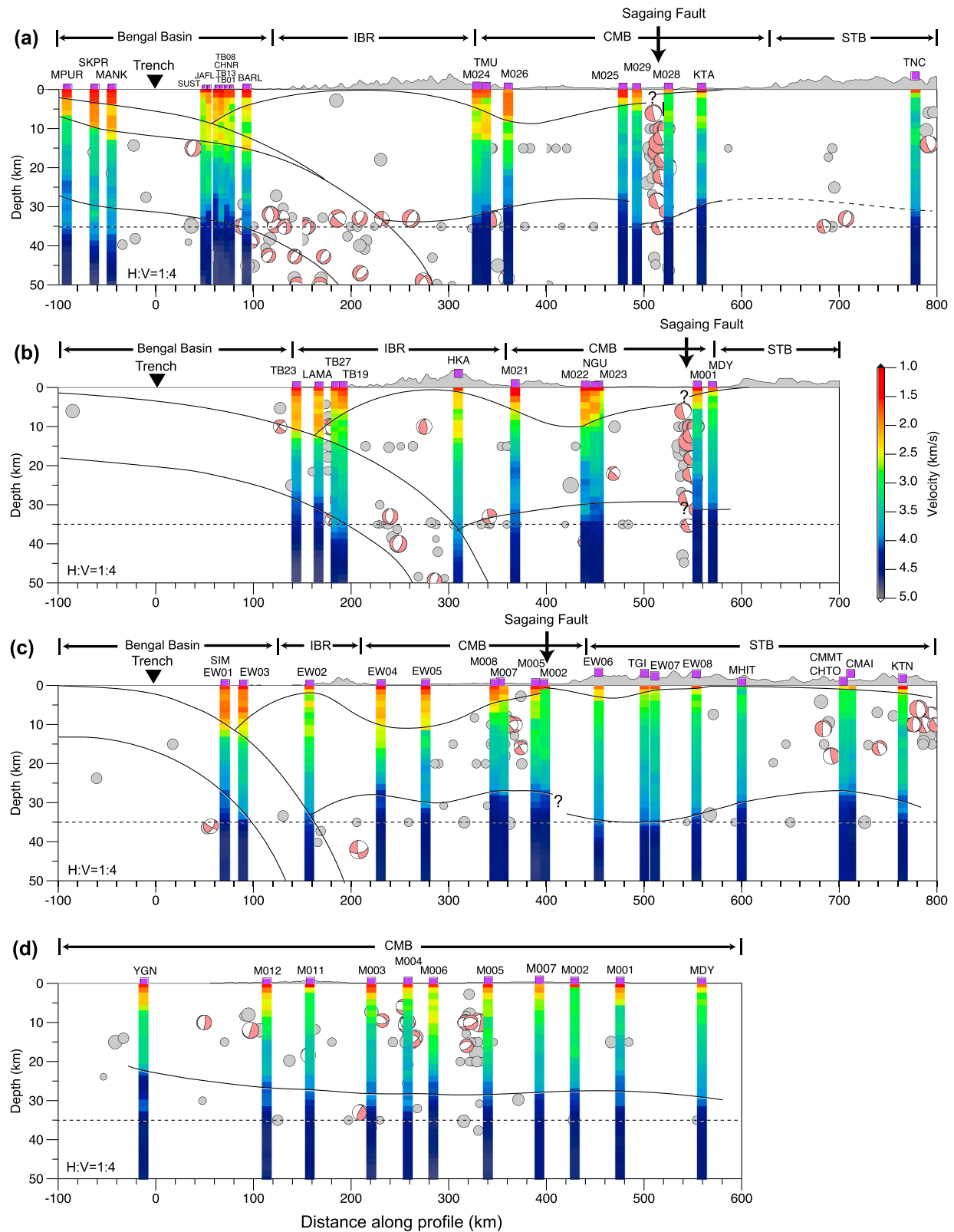## 5. One-Dimensional Velocity Profiles Beneath Each Station

Using the RF waveforms, H/V ratio, and SWD measurements, we apply the joint inversion scheme described earlier to all of the stations shown in Figure 1. The joint inversion results are displayed in Figure 7, shown as station-based 1-D velocity models along four profiles, as indicated by the dashed lines in Figure 1. The fits to the RF waveforms, H/V amplitude ratio, and SWD measurements predicted by the posterior mean velocity model are given in the supporting information (Figure S11).

Overall, the resulting velocity profiles beneath different stations show a highly variable crustal structure in Myanmar region, for both the shallow sedimentary structure and the Moho depth. At shallow depths, the station-based velocity models show excellent correlation with the surface geology. One of the most prominent features is the extremely thick low-velocity zone within the CMB, that is, at stations EW04, EW05, M022, and M026. The thick sedimentary layer can be directly inferred from the data, where broad and delayed first P arrivals in the RF waveforms and high H/V amplitude ratios of Rayleigh waves are observed (Lin et al., 2012; Yeck et al., 2013; Figure S11). As shown in our results, the basin thickness beneath these stations can be roughly estimated as 15 km, where the shear wave velocity increases from ~2.5 to ~3.0 km/s. It appears that the Sagaing fault lies very close to CMB's eastern boundary, with its surface trace transecting through the Cenozoic basin sediments. Across the IBR, in Bangladesh, the Bengal basin is around 10–15 km deep. In contrast, the STB, located to the east of the Sagaing fault, displays negligible sediment cover, with shallow shear wave velocities of ~3.0–3.5 km/s.

It is worth noting that we observe localized velocity reversals at some stations, for example, TB01, CHNR, TB13, BARAL, and TB08, where a low-velocity layer exists at ~10-km depth sandwiched by two high-velocity layers beneath and above it (Figure 7a). All of these stations are located within the Bengal Basin and IBR, and the thickness of the low-velocity layer decreases from the west to the east. Judging from the depth of this low velocity zone, and its eastward thinning and dipping feature, we suggest that this low-velocity zone might represent the downgoing Bengal basin sediments carried by the oblique subduction process between the Indian and the Burma Plate along the very gentle subduction interface (Steckler et al., 2016).

We also observe a clear shear wave velocity jump from ~3.5 to ~4.5 km/s at the depth range of 30–40 km, corresponding to the Moho interface between the crust and upper mantle. The average Moho depth beneath the CMB is ~30 km. We observe a significant change in Moho depth at stations crossing the Sagaing-Shan Scarp fault system. The Moho depth jumps from ~30 km in the CMB (west) to ~35 km close to the STB (east; Figures 7a and 7c). This change is well constrained as the profile has several stations on both sides of the Mogok Metamorphic Belt, which defines the edge of the STB. At the junction of the CMB and IBR, the Moho interface is not well identified (e.g., EW02 and HKA), as the velocity increases gradually from the crust to the mantle. Further to the west beneath the Bengal Basin, the Moho is clearer, with a depth of ~35 km. Based on these 1-D station-based models, we define the Moho depth as the largest velocity gradient where the shear wave velocity changes from ~3.5 to ~4.5 km/s. We then smoothly interpolate in order to draw the first-order Moho geometry (thin solid black lines) along four profiles, as shown in Figure 7.

Our results show ~5-km depth change of Moho across the Sagaing-Shan Scarp fault system, where the crustal thickness increases from ~30 km beneath Burma plate to ~35 km beneath STB (Figures 7a and 7c). The thicker crust of STB is not unexpected, as the age of STB is much older (Paleozoic) than the Burma Plate (Mesozoic to Cenozoic), and the STB elevation is also higher (~1,100 m) than the CMB (~200 m). The Moho offset is not located exactly beneath the Sagaing fault, which is considered as plate boundary type of fault. In profile A, the Moho offset takes place to the west of the Sagaing Fault. In contrast, profile C shows that the Moho offset is located to the east of the Sagaing fault, within the STB at its western edge. If we define the downdip fault geometry of the Sagaing fault as the connection of its surface trace and the Moho offset position, our observations would indicate that the fault is dipping strongly to the west in profile A and dipping to the east in profile C. However, this is inconsistent with the background seismicity from the global seismic catalogue (Figures 1 and 7), which line up near vertically and have near vertical fault plane solutions. These seismicity includes the Mw 6.8 earthquake occurred in 2012, just south of the profile A, that has a subvertical fault that slightly dips to east (Figure 7). Therefore, the Moho offset location is not located on the active Sagaing fault; instead, it is probably a signature of an older plate-boundary fault system (i.e., Shan-Scarp Fault system).

AGU
100
ADVANCING EARTH
AND SPACE SCIENCE

Journal of Geophysical Research: Solid Earth

10.1029/2018JB016622

Figure 7. Velocity profiles from joint inversion for each station, projected onto schematic tectonic profiles (see Figure 1 for locations). Background seismicity within 50 km of the profiles is shown, and the topography and geological regions are indicated. The width of the bar graphs beneath the stations are narrowed below the eastern Bengal basin in profile (a) to accommodate the dense stations (Figure 7a). First-order structural features have been outlined with thin black lines. A less vertically stretched version of the figure with depth down to 80 km is shown in Figure S12.

We do not see Moho offset in profile B, this could be due to the easternmost station (MDY) is located only ~10 km to the east of the Sagaing fault, and the actual Moho offset should be located even further to the east. If indeed, the Moho discontinuity is associated to an older, inactive plate-boundary fault system, we expect the Moho offset would appear within the STB. Interestingly, an earlier geodetic observation near our profile B suggests the center of the dislocation model is located ~17 km to the east of the active Sagaing fault trace (Vigny et al., 2003). These observations imply that although the Moho discontinuity was likely generated by a much older structure than the Sagaing fault, it may still play a role in modulating current fault activity and deformation of the Sagaing fault system. The spatial variation of the Moho depth across the Shan-Sagaing Scarp fault system, and its relationship to the modern seismicity could be investigated in greater detail in the future with a much denser seismic network.

6. Constructing an Integrated 3-D Velocity Model

In this section, we interpolate the station-based 1-D velocity profiles to construct an integrated 3-D velocity model, which is essential for a series of seismological studies, for example, earthquake location determinations and focal mechanism inversions.

Due to the limited number of stations used in this study (Figure 1), we use a hybrid approach that integrates our preferred 1-D velocity profiles and the global CRUST 1.0 model to construct a 3-D velocity model. We mesh the study region into a 0.5° by 0.5° grid. We then calculate the distance of each grid cell to the closest station. For grid cells with no station within 100 km, such as in the ocean, at the edge of the study region and in some parts of the STB, we use the CRUST 1.0 model; otherwise, we use the station-based velocity models that we have calculated for this grid point (Figure S13). The grid values are then smoothed and interpolated using the *surface* command in Generic Mapping Tools (GMT; Wessel et al., 2013). The integrated 3-D velocity model, named Myanmar Hybrid version1 (Myanmar_H_v1), has better resolution within central Myanmar, where we have a denser station distribution than in other model regions. Map view of the 3-D model at different depth are presented in Figure 8. A detailed comparison of our new velocity model with CRUST 1.0 model (Laske et al., 2013) can be found in the supporting information (Figures S14 and S15).

7. Discussion

7.1. Comparison With Previous RF Inversion Studies

To verify our results, we select two stations, IU.CHTO and XI.SUST, which have been previously analyzed, and compare our results with previous studies.

Station IU.CHTO, a borehole broadband station located in Thailand that has been in operation for more than 10 years and that has recorded a large volume of high-quality data. Both the RFs and H/V ratio derived from these data show small uncertainties (Figure 9a), although the SWD measurements display larger uncertainties due to the limited number of nearby stations (Figures 9a and S5–S10). Through the joint inversion, we can fit all three measurements well. Our preferred velocity model indicates a smooth Moho, where the transition of shear wave speeds from 3.7 to 4.5 km/s take place across a depth range of 10 km with an average depth of 25 km (Figure 9a). In Figure 9c, we plot our joint inversion model together with the models derived from other RF waveform inversions (Bai et al., 2010; Hu et al., 2008; Noisagool et al., 2016). Overall, our model is consistent with previous studies, except at shallow depths (5–10 km), where our preferred velocity model shows a slightly lower shear wave speed (~2.7 km/s) than the other models (~3.1 km/s). This discrepancy is probably due to the additional constraints from the H/V ratio and SWD. The H/V ratio and SWD measurements are sensitive to a larger volume of structure around the seismic station (Maupin, 2017), in contrast to higher-frequency body waves, which are sensitive to the structure along the raypath. To further understand the contribution of the H/V ratio and SWD in the inversion, we calculate the theoretical H/V ratio and SWD using the velocity models from Bai et al. (2010), Hu et al. (2008), and Noisagool et al. (2016) and compare them with the observations. As shown in Figure S16a, the joint inversion can fit the data much better than those models, indicating that the H/V ratio and SWD bring important constrains to the velocity structure beneath the station.

We conducted a similar comparison for station XI.SUST, which is a temporary station located within the Bengal Basin that was operated for one and a half years. Due to the site conditions and the relatively
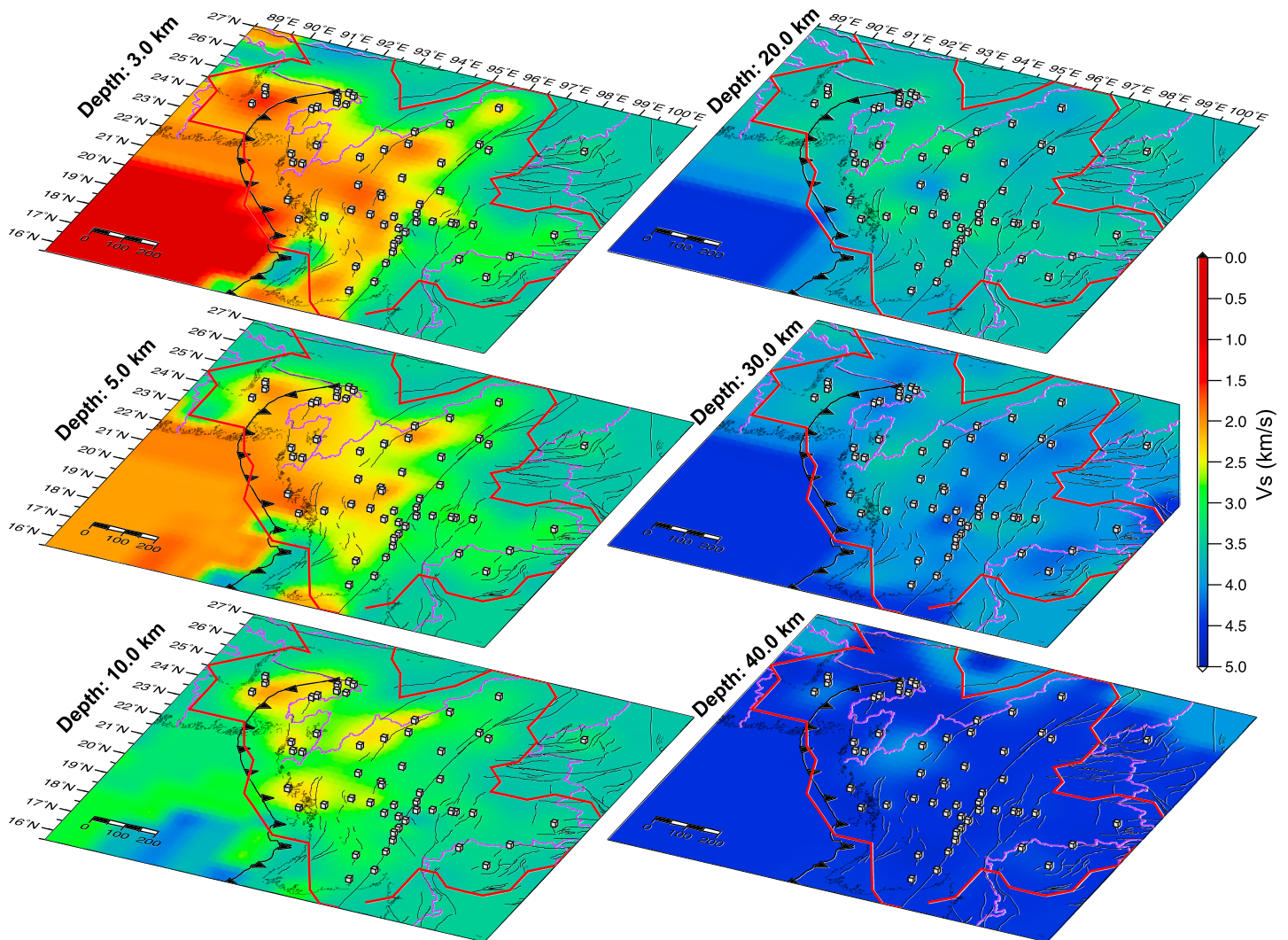
Figure 8. Map view of the shear wave speed of the proposed 3-D model at different depth. The depth for each map is marked in the upper-left corner of each panel. The red polygon indicates our hybrid approach, where the inner and outer of polygon are mainly constrained from our station-based 1-D velocity profiles and the CRUST 1.0 model, respectively. More details about hybrid approach can be found in Figure S13.

short operational period, both the RFs and H/V ratio show larger uncertainties than station IU.CHTO (Figures 9d and 9e). The RFs waveforms show a clear delayed and broadened direct P phase (Figure 9d), suggesting strong basin effects (Yeck et al., 2013). Our inversion reveals a very low velocity zone with shear wave speeds less than 2.0 km/s at shallow (<3 km) depth, which is consistent with previous studies (Mitra et al., 2018; Singh et al., 2016). At depths of 5 to 15 km, the average shear wave speed is also relatively low (~2.5 km/s), which suggests that the lithology is still sedimentary. This shear wave speed is similar to that of Singh et al. (2016) but much lower than that from Mitra et al. (2018). The middle and lower crustal structure shows quite a large difference among these three models (Figure 9f). To further verify these models, we compute the synthetic RF waveform, H/V ratio, and SWD generated using different velocity models and compare them with the real data (Figure S16b). For the H/V ratio, neither Singh et al.'s (2016) nor Mitra et al.'s (2018) model can fit the measurements as well as our preferred model. For the RF waveforms, Singh et al.'s (2016) model is too simple to capture the complicated waveforms (Figure S16b), and Mitra et al.'s (2018) model produces a large amplitude ratio between the direct P wave and the following phases at 3.5 s, which does not fit the data. These simple forward modeling tests indicate the importance of using multiple data sets to constrain a velocity model through a joint inversion.
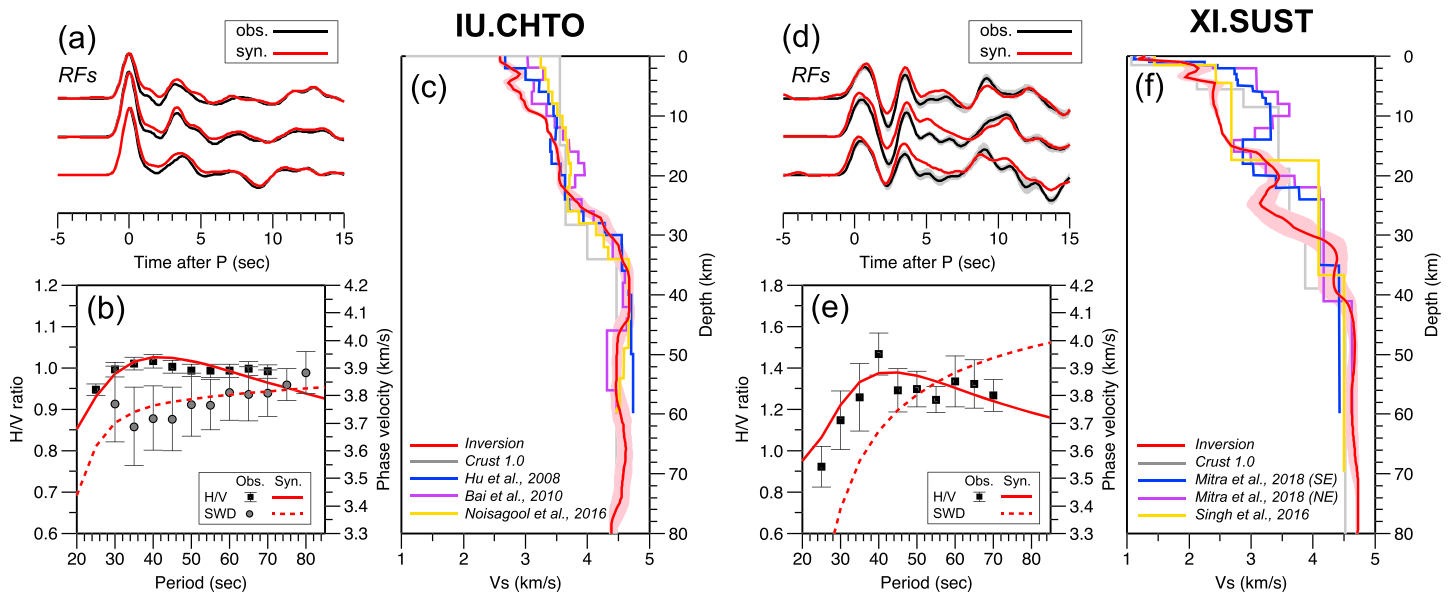
Figure 9. Comparison between our inversion and previous studies for stations IU.CHTO (a–c) and XI.SUST (d–f). (a) Receiver function (RF) waveforms fits. The black and red lines show RF observations and the synthetic RFs from joint inversion. (b) H/V ratio and surface wave dispersion (SWD) fits, where the squares and circles indicates the H/V ratio and SWD measurement, respectively. The solid and dashed red lines indicate the results from joint inversion. (c) Our preferred velocity model, CRUST 1.0 model and the results from previous studies. (d–f) The same but for station XI.SUST.
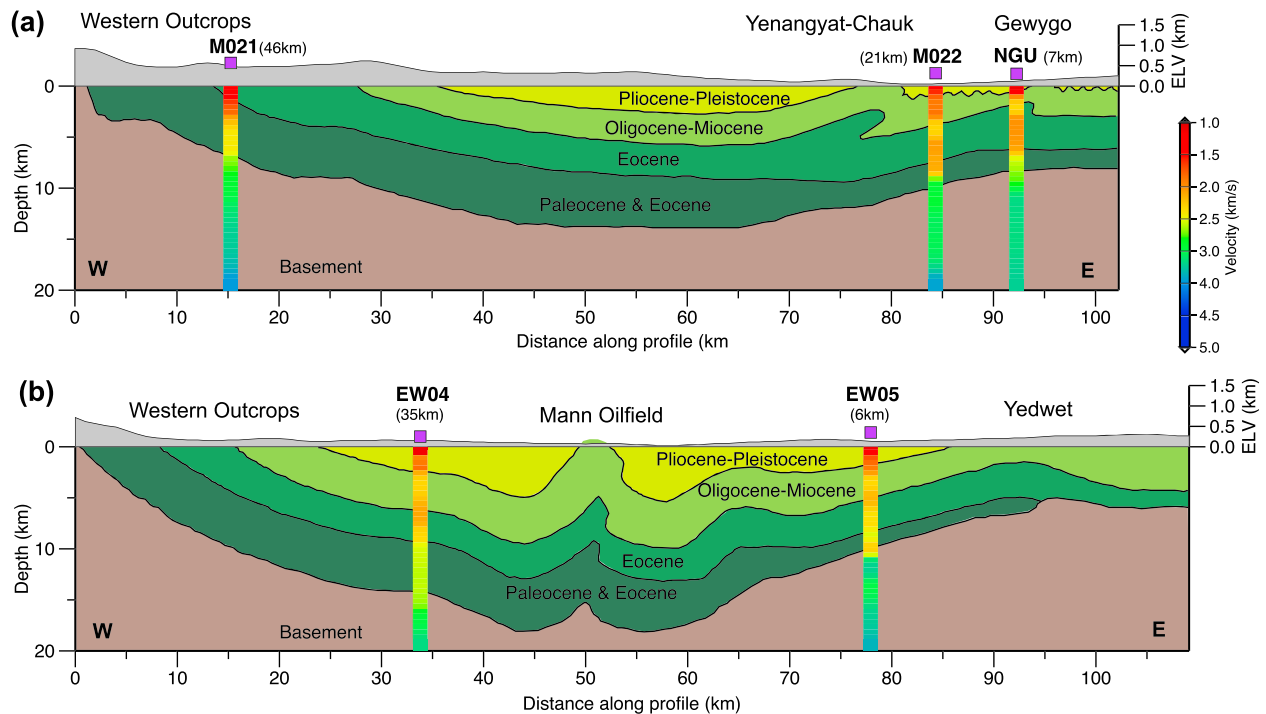
7.2. Comparison With Geological Cross Sections

To further verify our velocity models, especially at shallow depths, we compare our results with two previous published geological cross sections (Pivnik et al., 1998; Ridd & Racey, 2015) that were produced by interpreting industrial seismic reflection profiles, well logs, aeromagnetic data, and surface geology. These two cross sections overlap or are very close to our seismic stations (red lines in Figure 1), providing a detailed picture of the basin geometry and layered structure within the basin. Note that the deepest part of the basin in the profiles is around 18 km, interpreted as Eocene sedimentary rocks. Figure 10 shows a comparison of our 1-D profiles with the structural cross sections. The depth of the basin in our models, defined as 2.5 km/s, agrees remarkably well with the basin depth in the cross section, supporting the robustness of our inversion results. We note that the shallow part of the basin, interpreted to be filled with young Irrawaddy sediment (Pliocene-Pleistocene; Pivnik et al., 1998), has a shear wave speed of 1.0–2.0 km/s in our model.

7.3. Model Assessment Using Regional 3-D Waveform Simulation

In this section, we use 3-D waveform simulation to directly assess the performance of our velocity model compared to CRUST 1.0 model (Laske et al., 2013). In order to use our proposed 3-D velocity model (Figure 8) in 3-D waveform simulations, we interpolate the 0.5° × 0.5° model spacing to the grid spacing that is necessary for simulation meshing. We collect the waveform data from three medium size earthquakes, 7 January 2018 Yairipok (Mw 5.6), 11 January 2018 Pyu (Mw 6.0), and 7 March 2018 NayPyiTaw (Mw 4.7), which were located in northern, southern, and central Myanmar (Figure 1), respectively. We use a point source focal mechanism for each of the events, compute 3-D synthetic seismograms, and compare them with the observations, to evaluate the performance of our velocity model and the CRUST 1.0 model.

The 11 January 2018 Mw 6.0 Pyu earthquake in southern Myanmar is one of the recent earthquakes well recorded by our network. The earthquake also generated good SNR teleseismic records due to its size. The earthquake produced more than 10-cm line-of-sight deformation in interferometric synthetic aperture radar (InSAR) images, providing a very accurate earthquake location and centroid depth (~5 km). To derive a focal mechanism and centroid depth of this earthquake for 3-D simulations, we apply a long-period cut-and-paste inversion algorithm to the teleseismic P and SH waves (Wang et al., 2017; Figure S17). We do not use regional waveform in the inversion because we use them later to evaluate our model. The inversion yields a thrust mechanism (strike 350°/158°, dip 34°/57°, and rake 100°/83°) with a centroid depth around 8 km

Figure 10. Comparison between our results and geological cross sections. Geological cross sections are modified from Pivnik et al. (1998) and Ridd and Racey (2015). The locations of the profiles are given as red lines in Figure 1. Nearby stations have been projected onto the profiles, with the distance to the profile shown near the station name in parentheses.

(Figure S17). The uncertainties estimated from the bootstrapping method suggest that the fault plane solution is well constrained (Figure S17).

Using the source parameters obtained by teleseismic waveform data, we then perform regional 3-D waveform simulations using the spectral element method (Komatitsch & Tromp, 1999) for our new model (Myanmar_H_v1) and the CRUST 1.0 model. In our spectral element method simulations, we use spherical coordinates and include the surface topography. The horizontal grid size is around 5 km and the vertical grid size varies from ~8 km in the upper mantle to about 2.5 km in the lower crust and further reduces to ~1 km in the shallowest sediments (Figure S18), resulting in a numerical accuracy of up to 2 s. In our simulations, the earthquake centroid depth (5 km) is derived by fitting the InSAR data, which are more sensitive to the slip distribution compared with long-period teleseismic data. We also vary the focal depth from 5 to 10 km to search for the best depth. We find that a centroid depth of 5-km fits the regional data best, consistent with the centroid depth from InSAR data.

Figure 11 shows a comparison between the observed and 3-D synthetic seismograms, in a fashion of the cut-and-paste method (Zhu & Helmberger, 1996), in which the seismograms are separated into *Pnl* and surface wave portions. In general, both models fit the *Pnl* waves well, up to 0.15 Hz, where most of the stations have CCCs between data and synthetics of around 70% (Figures 11, 12a, and 12d). At a few stations (e.g., EW02, EW04, and EW06), our 3-D model fits the data much better than CRUST 1.0, in particular for the surface waves. It is clear that for these stations, the CRUST 1.0 synthetics show much lower amplitudes than the data, while our 3-D model matches the data amplitude and waveforms much better (Figure 11). The amplitude mismatch is not likely to be caused by an error in the moment magnitude, as *Pnl* waves amplitudes are fit well by both models, and the surface wave amplitude from CRUST 1.0 fits the data well at some of the stations (e.g., M002, M001, and M023 in Figure 11). The amplitude mismatch is also not caused by the error in focal mechanism, which was robustly determined by teleseismic and InSAR data. The waveform CCC from our model is also much better than that from CRUST 1.0 (Figures 12b–12f). The 3-D effect is very clear in our model; for instance, at station M022, despite large surface wave amplitudes in the observations, the CRUST 1.0 synthetics have near-zero amplitudes for both Love and Rayleigh waves (Figure 11), which
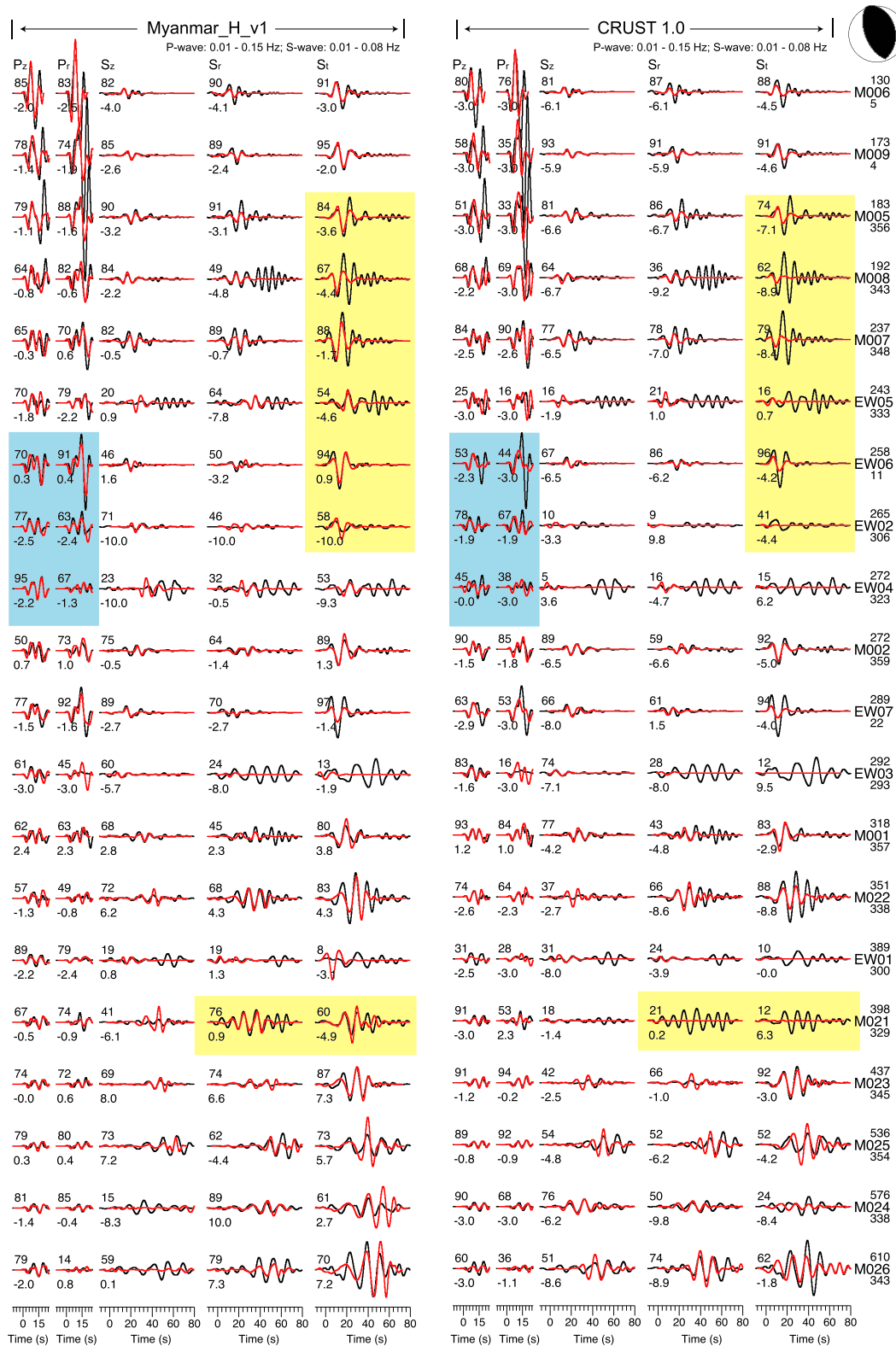
Figure 11. Waveform comparison between the real data and synthetics obtained using our velocity model (left panel) and the CRUST 1.0 model (right panel). In each panel, the waveforms have been divided into *Pnl* waves in vertical and radial components (*Pz/Pr*), *SV* or Rayleigh waves in vertical and radial components (*Sz/Sr*) and *SH* or Love waves in tangential components (*St*). The *Pz/Pr* and *Sz/Sr/St* have been filtered to 0.01–0.15 Hz and 0.01–0.08 Hz, respectively. Black traces are observed waveforms and red traces are 3-D synthetics. The number above and below each waveform pair are the waveform cross correlation as a percentage and the time shifts in seconds. The station name is indicated at the right side, with epicentral distance and azimuth shown above and below the station name.
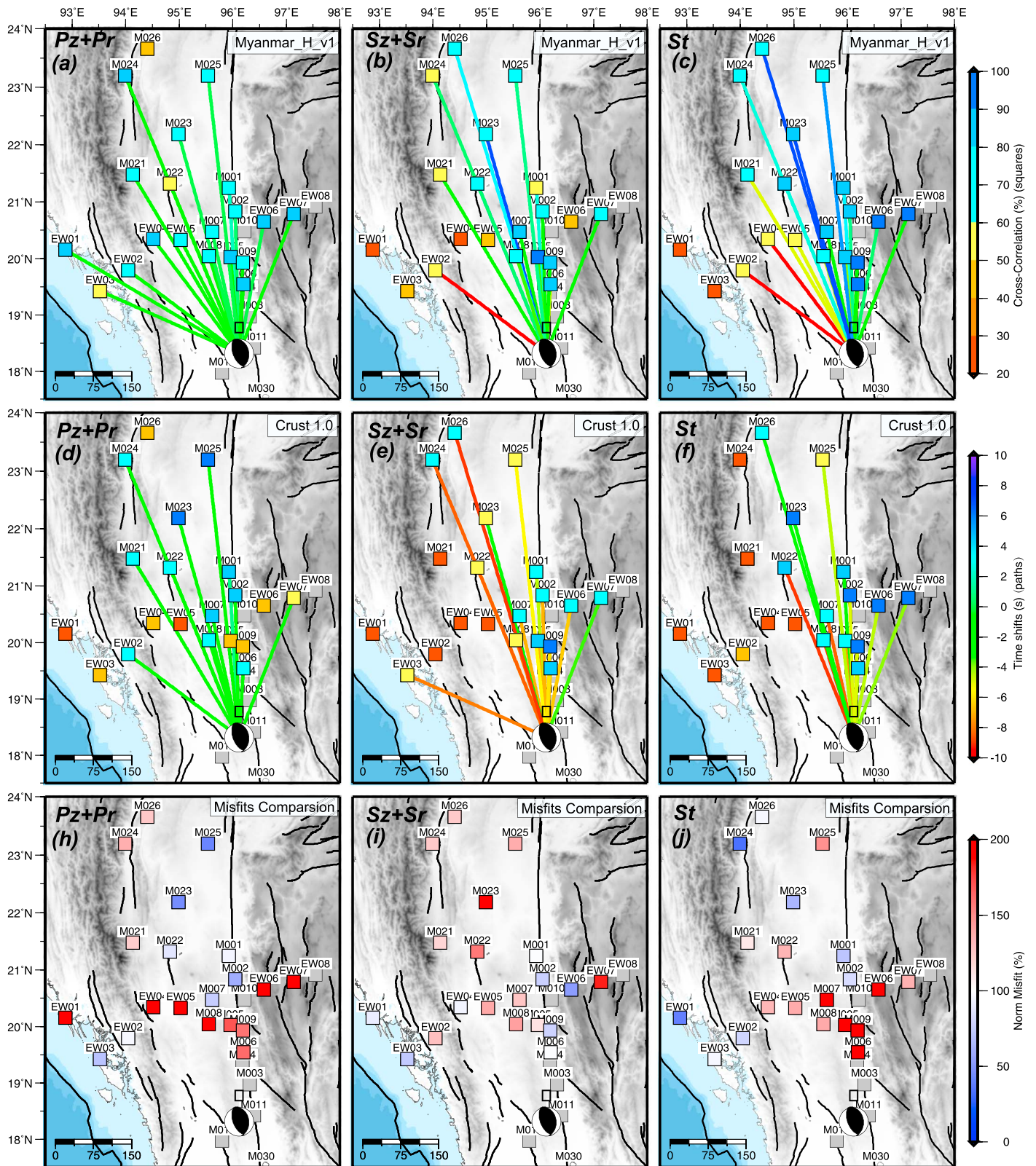
Figure 12. Spider diagrams of the *P* wave (a)/(d), Raleigh wave (b)/(e), and Love wave (c)/(f) time shifts between real data and synthetics using our new velocity model (a–c) and the CRUST 1.0 model (d–f). The colors of the paths indicate the time shifts, and the station colors indicate the CCCs. Here we only show the time shifts of stations with CCC > 50, as the time shifts obtained from low CCC data are not meaningful. (h–j) The misfit comparison between our velocity model and CRUST 1.0 model. The definition of the misfits can be found in section 7.3.

suggests that the station is located toward the nodal plane of the surface waves. In contrast, our model generates much better waveform fits (Figure 11, station M21), indicating strong off-plane multipathing effects caused by the basin structure. To further quantify the performance of our proposed velocity model, we compare the CCCs, time shifts, and relative misfits in Figure 12. For central Myanmar stations, the average time shift of the surface waves computed using the CRUST 1.0 model is around -7 s (negative means that the model is faster than the real Earth), whereas this value is much smaller (around -2 s) in our model. For the stations in northern Myanmar, the time shifts show large positive values (around $+6$ s), which is likely due to the relatively poor resolution of the velocity model, as the stations in northern Myanmar are sparse. To better compare the misfit from different models, we also define the relative misfit (e) as $e = Misfit_{CRUST}/Misfit_{Myanmar\_H\_v1}$, where $Misfit = \|obs(t) - syn(t - dt)\|^2$ indicates the L2 normal error between the data and the shifted synthetics. For most of the stations, the synthetics from the CRUST 1.0 model show larger misfits than those from our integrated 3-D velocity model (Figures 12h and 12i). The comparison of the other two earthquakes, which are located in central and northern Myanmar, respectively, also show better waveform fits using our 3-D velocity model than CRUST 1.0. More details of the comparisons are given in the supporting information (Figures S19–S23).

In short, through various verifications and evaluations, we show that our integrated 3-D velocity model performs better than the CRUST 1.0 model for most of the stations in Myanmar. This highlights the potential utility of our velocity model for a variety of seismological and seismic hazard applications in Myanmar, including earthquake location determinations, focal mechanism inversions, and ground motion simulations.

7.4. Limitations of the Current Study and Potential Refinements in the Future

Prior to this study, little was known about the crustal-scale velocity structure of Myanmar. Here we obtain station-based 1-D shear velocity models for 56 stations in and around Myanmar, we also interpolate these 1-D models and combine with the CRUST 1.0 model to generate a 3-D shear wave velocity model for the Myanmar region. However, given relatively sparse station distribution, current velocity models are considered as preliminary results and further improvements can be foreseen.

During our data processing, the RF waveforms were filtered at ~0.75 Hz (corresponding to a Gaussian parameter of 1.5), and the H/V ratio and SWD were measured at 25–70 s and 30–80 s, respectively. For the RF waveform data, 0.75 Hz is relatively low frequency compared with other typical crustal-scale RF studies; thus, the inversion focus more on the first-order crustal scale velocity structures. A potential improvement of the RF inversion could be to include multifrequency RF waveforms in the inversion to simultaneously capture multiscale features in the structure (Chong et al., 2017; Li et al., 2017). For the H/V ratio and SWD measurements, the minimum period used in the inversion is around ~30 s, due to earthquake-based measurements and sparse station distribution (Jin & Gaherty, 2015; Romanowicz, 2002; Tanimoto & Rivera, 2008). Besides, there is no SWD measurements in Bangladesh and IBR, as the operation period of stations in these regions did not overlap with the rest of the network. Thus, our joint inversions have relatively weak constraints on the absolute velocity structure in Bangladesh and IBR. To use shorter-period measurements in the inversion to improve the resolution, ambient noise cross correlation is a good complementary data set to be included in the future. In addition, travel time tomography using local and regional earthquake data will provide better constraints to the deeper structure. Note that we have used waveform records of three regional earthquakes in forward modeling, given very active seismicity in the region, waveform tomography will become more feasible as the volume of data increases. In any case, more stations are always helpful and collaborations between institutes and scientists will greatly improve the efficiency. Last but not least, another way to compensate for seismic station sparsity is to include gravity and surface geology data that usually have good spatial coverage to provide additional constraints to the 3-D velocity model.

8. Conclusions

In this study, we estimate 1-D station-based shear velocities beneath 56 stations in and around Myanmar through joint inversion of RFs, H/V ratio, and SWD measurements using a transdimensional McMC Bayesian approach. The resulting velocity profile beneath each station shows highly variable crustal structure across Myanmar. At shallow depths, our model shows excellent correlation with the surface geology

and reveals the first-order basin geometry, which has depths of up to 15 km of sediment. At greater depths, we find that the Moho depth is around 30 km beneath the CMB, while there is significant Moho offset across the Sagaing-Shan Scarp fault system in central Myanmar, where the depth increases from ~30 to ~35 km under the STB. We also use 3-D waveform simulations to compare our velocity model with the CRUST 1.0 model. Synthetic seismograms computed using our model for three regional earthquakes show systematically better waveform fits to the real data than those computed using the CRUST 1.0 model. Seismic velocity models obtained in this study can be found in supporting information. Our preferred velocity model provides a preliminary community velocity model for the region, which can be used for a variety of seismological and geological applications and investigations.

References

Agostinetti, N. P., & Malinverno, A. (2010). Receiver function inversion by trans-dimensional Monte Carlo sampling. *Geophysical Journal International*, *181*(2), 858–872.

Ammon, C. J. (1991). The isolation of receiver effects from teleseismic P waveforms. *Bulletin of the Seismological Society of America*, *81*(6), 2504–2510.

Bai, L., Tian, X., & Ritsema, J. (2010). Crustal structure beneath the Indochina peninsula from teleseismic receiver functions. *Geophysical Research Letters*, *37*, L24308. https://doi.org/10.1029/2010GL044874

Bao, X., Sun, X., Xu, M., Eaton, D. W., Song, X., Wang, L., et al. (2015). Two crustal low-velocity channels beneath SE Tibet revealed by joint inversion of Rayleigh wave dispersion and receiver functions. *Earth and Planetary Science Letters*, *415*, 16–24. https://doi.org/10.1016/j. epsl.2015.01.020

Bensen, G., Ritzwoller, M., Barmin, M., Levshin, A., Lin, F., Moschetti, M., et al. (2007). Processing seismic ambient noise data to obtain reliable broad-band surface wave dispersion measurements. *Geophysical Journal International*, *169*(3), 1239–1260. https://doi.org/ 10.1111/j.1365-246X.2007.03374.x

Bodin, T., Sambridge, M., Tkalčić, H., Arroucau, P., Gallagher, K., & Rawlinson, N. (2012). Transdimensional inversion of receiver functions and surface wave dispersion. *Journal of Geophysical Research*, *117*, B02301. https://doi.org/10.1029/2011JB008560

Box, G. E., & Tiao, G. C. (2011). *Bayesian inference in statistical analysis*. New York: John Wiley & Sons. https://doi.org/10.1002/9781118033197

Brocher, T. M. (2005). Empirical relations between elastic wavespeeds and density in the Earth's crust. *Bulletin of the Seismological Society of America*, *95*(6), 2081–2092. https://doi.org/10.1785/0120050077

Chong, J., Chu, R., Ni, S., Meng, Q., & Guo, A. (2017). Receiver function HV ratio: A new measurement for reducing non-uniqueness of receiver function waveform inversion. *Geophysical Journal International*, *212*(2), 1475–1485.

Chong, J., Ni, S., Chu, R., & Somerville, P. (2016). Joint inversion of body-wave receiver function and Rayleigh-wave ellipticity. *Bulletin of the Seismological Society of America*, *106*(2), 537–551. https://doi.org/10.1785/0120150075

Crotwell, H. P., Owens, T. J., & Ritsema, J. (1999). The TauP toolkit: Flexible seismic travel-time and ray-path utilities. *Seismological Research Letters*, *70*(2), 154–160. https://doi.org/10.1785/gssrl.70.2.154

Dettmer, J., Dosso, S. E., & Holland, C. W. (2010). Trans-dimensional geoacoustic inversion. *The Journal of the Acoustical Society of America*, *128*(6), 3393–3405. https://doi.org/10.1121/1.3500674

Dziewonski, A. M., & Anderson, D. L. (1981). Preliminary reference earth model. *Physics of the Earth and Planetary Interiors*, *25*(4), 297–356. https://doi.org/10.1016/0031-9201(81)90046-7

Efron, B., & Tibshirani, R. (1991). Statistical data analysis in the computer age. *Science*, *253*(5018), 390–395. https://doi.org/10.1126/ science.253.5018.390

Ekstrom, G., Nettles, M., & Dziewonski, A. M. (2012). The global CMT project 2004-2010: Centroid-moment tensors for 13,017 earthquakes. *Physics of the Earth and Planetary Interiors*, *200-201*, 1–9. https://doi.org/10.1016/j.pepi.2012.04.002

Engdahl, E. R., van der Hilst, R., & Buland, R. (1998). Global teleseismic earthquake relocation with improved travel times and procedures for depth determination. *Bulletin of the Seismological Society of America*, *88*(3), 722–743.

Gardiner, N. J., Robb, L. J., Morley, C. K., Searle, M. P., Cawood, P. A., Whitehouse, M. J., et al. (2016). The tectonic and metallogenic framework of Myanmar: A Tethyan mineral system. *Ore Geology Reviews*, *79*, 26–45. https://doi.org/10.1016/j.oregeorev.2016.04.024

Green, P. J. (1995). Reversible jump Markov chain Monte Carlo computation and Bayesian model determination. *Biometrika*, *82*(4), 711–732. https://doi.org/10.1093/biomet/82.4.711

Green, P. J. (2003). Trans-dimensional Markov chain Monte Carlo. *Oxford Statistical Science Series*, *27*, 179–198.

Hopcroft, P. O., Gallagher, K., & Pain, C. C. (2007). Inference of past climate from borehole temperature data using Bayesian reversible jump Markov chain Monte Carlo. *Geophysical Journal International*, *171*(3), 1430–1439. https://doi.org/10.1111/j.1365-246X.2007.03596.x

Hu, J., Yang, H., & Zhao, H. (2008). Structure and significance of S-wave velocity and Poisson's ratio in the crust beneath the eastern side of the Qinghai-Tibet Plateau. *Pure and Applied Geophysics*, *165*(5), 829–845. https://doi.org/10.1007/s00024-008-0336-6

Hurukawa, N., & Maung Maung, P. (2011). Two seismic gaps on the Sagaing Fault, Myanmar, derived from relocation of historical earthquakes since 1918. *Geophysical Research Letters*, *38*, L01310. https://doi.org/10.1029/2010GL046099

Hurukawa, N., Tun, P. P., & Shibazaki, B. (2012). Detailed geometry of the subducting Indian plate beneath the Burma plate and subcrustal seismicity in the Burma plate derived from joint hypocenter relocation. *Earth, Planets and Space*, *64*(4), 333–343. https://doi.org/ 10.5047/eps.2011.10.011

Jin, G., & Gaherty, J. B. (2015). Surface wave phase-velocity tomography based on multichannel cross-correlation. *Geophysical Journal International*, *201*(3), 1383–1398. https://doi.org/10.1093/gji/ggv079

Komatitsch, D., & Tromp, J. (1999). Introduction to the spectral element method for three-dimensional seismic wave propagation. *Geophysical Journal International*, *139*(3), 806–822. https://doi.org/10.1046/j.1365-246x.1999.00967.x

Langston, C. A. (1979). Structure under Mount Rainier, Washington, inferred from teleseismic body waves. *Journal of Geophysical Research*, *84*(NB9), 4749–4762. https://doi.org/10.1029/JB084iB09p04749

Laske, G., G. Masters, Z. Ma, and M. Pasyanos (2013). Update on CRUST1. 0—A 1-degree global model of Earth's crust.

Li, C., Van der Hilst, R. D., Meltzer, A. S., & Engdahl, E. R. (2008). Subduction of the Indian lithosphere beneath the Tibetan Plateau and Burma. *Earth and Planetary Science Letters*, *274*(1–2), 157–168. https://doi.org/10.1016/j.epsl.2008.07.016

Li, G., Chen, H., Niu, F., Guo, Z., Yang, Y., & Xie, J. (2016). Measurement of Rayleigh wave ellipticity and its application to the joint inversion of high-resolution S wave velocity structure beneath Northeast China. *Journal of Geophysical Research: Solid Earth*, *121*, 864–880. https://doi.org/10.1002/2015JB012459

Li, X., Li, Z., Hao, T., Wang, S., & Xing, J. (2017). A multi-frequency receiver function inversion approach for crustal velocity structure. *Computational Geosciences*, *102*, 45–55. https://doi.org/10.1016/j.cageo.2017.02.009

Ligorría, J. P., & Ammon, C. J. (1999). Iterative deconvolution and receiver-function estimation. *Bulletin of the Seismological Society of America*, *89*(5), 1395–1400.

Lin, F.-C., & Ritzwoller, M. H. (2011). Helmholtz surface wave tomography for isotropic and azimuthally anisotropic structure. *Geophysical Journal International*, *186*(3), 1104–1120. https://doi.org/10.1111/j.1365-246X.2011.05070.x

Lin, F.-C., Ritzwoller, M. H., & Snieder, R. (2009). Eikonal tomography: Surface wave tomography by phase front tracking across a regional broad-band seismic array. *Geophysical Journal International*, *177*(3), 1091–1110. https://doi.org/10.1111/j.1365-246X.2009.04105.x

Lin, F. C., Schmandt, B., & Tsai, V. C. (2012). Joint inversion of Rayleigh wave phase velocity and ellipticity using USArray: Constraining velocity and density structure in the upper crust. *Geophysical Research Letters*, *39*, L12303. https://doi.org/10.1029/2012GL052196

Long, M. D. (2013). Constraints on subduction geodynamics from seismic anisotropy. *Reviews of Geophysics*, *51*, 76–112. https://doi.org/10.1002/rog.20008

Luo, X. (2010). Constraining the shape of a gravity anomalous body using reversible jump Markov chain Monte Carlo. *Geophysical Journal International*, *180*(3), 1067–1079. https://doi.org/10.1111/j.1365-246X.2009.04479.x

Malinverno, A. (2002). Parsimonious Bayesian Markov chain Monte Carlo inversion in a nonlinear geophysical problem. *Geophysical Journal International*, *151*(3), 675–688. https://doi.org/10.1046/j.1365-246X.2002.01847.x

Malinverno, A., & Briggs, V. A. (2004). Expanded uncertainty quantification in inverse problems: Hierarchical Bayes and empirical Bayes. *Geophysics*, *69*(4), 1005–1016. https://doi.org/10.1190/1.1778243

Malinverno, A., & Parker, R. L. (2006). Two ways to quantify uncertainty in geophysical inverse problems. *Geophysics*, *71*(3), W15–W27. https://doi.org/10.1190/1.2194516

Maupin, V. (2017). 3-D sensitivity kernels of the Rayleigh wave ellipticity. *Geophysical Journal International*, *211*(1), 107–119. https://doi.org/10.1093/gji/ggx294

Maurin, T., & Rangin, C. (2009). Structure and kinematics of the Indo-Burmese Wedge: Recent and fast growth of the outer wedge. *Tectonics*, *28*, TC2010. https://doi.org/10.1029/2008TC002276

Minsley, B. J. (2011). A trans-dimensional Bayesian Markov chain Monte Carlo algorithm for model assessment using frequency-domain electromagnetic data. *Geophysical Journal International*, *187*(1), 252–272. https://doi.org/10.1111/j.1365-246X.2011.05165.x

Mitra, S., Priestley, K., Borah, K., & Gaur, V. (2018). Crustal structure and evolution of the eastern Himalayan plate boundary system, Northeast India. *Journal of Geophysical Research: Solid Earth*, *123*, 621–640. https://doi.org/10.1002/2017JB014714

Ni, J. F., Guzman-Speziale, M., Bevis, M., Holt, W. E., Wallace, T. C., & Seager, W. R. (1989). Accretionary tectonics of Burma and the three-dimensional geometry of the Burma subduction zone. *Geology*, *17*(1), 68–71. https://doi.org/10.1130/0091-7613(1989)017<0068:ATOBAT>2.3.CO;2

Niu, F., & Li, J. (2011). Component azimuths of the CEArray stations estimated from P-wave particle motion. *Earthquake Science*, *24*(1), 3–13. https://doi.org/10.1007/s11589-011-0764-8

Noisagool, S., Boonchaisuk, S., Pornsopin, P., & Siripunvaraporn, W. (2016). The regional moment tensor of the 5 May 2014 Chiang Rai earthquake (Mw = 6.5), Northern Thailand, with its aftershocks and its implication to the stress and the instability of the Phayao Fault Zone. *Journal of Asian Earth Sciences*, *127*, 231–245. https://doi.org/10.1016/j.jseaes.2016.06.008

Obayashi, M., Yoshimitsu, J., Nolet, G., Fukao, Y., Shiobara, H., Sugioka, H., et al. (2013). Finite frequency whole mantle P wave tomography: Improvement of subducted slab images. *Geophysical Research Letters*, *40*, 5652–5657. https://doi.org/10.1002/2013GL057401

Pesicek, J. D., Thurber, C. H., Widiyantoro, S., Zhang, H., DeShon, H. R., & Engdahl, E. R. (2010). Sharpening the tomographic image of the subducting slab below Sumatra, the Andaman Islands and Burma. *Geophysical Journal International*, *182*(1), 433–453. https://doi.org/10.1111/j.1365-246X.2010.04630.x

Pivnik, D. A., Nahm, J., Tucker, R. S., Smith, G. O., Nyein, K., Nyunt, M., & Maung, P. H. (1998). Polyphase deformation in a fore-arc/back-arc basin, Salin subbasin, Myanmar (Burma). *AAPG Bulletin*, *82*(10), 1837–1856.

Ridd, M. F., & Racey, A. (2015). Onshore petroleum geology of Myanmar: Central Burma depression. *Geological Society, London, Memoirs*, *45*(1), 21–50. https://doi.org/10.1144/M45.04

Romanowicz, B. (2002). Inversion of surface waves: A review. *International Geophysics Series*, *81*(A), 149–174. https://doi.org/10.1016/S0074-6142(02)80214-5

Rueda, J., & Mezcua, J. (2015). Orientation analysis of the Spanish broadband national network using Rayleigh-wave polarization. *Seismological Research Letters*, *86*(3), 929–940. https://doi.org/10.1785/0220140149

Saito, M. (1988). DISPER80: A subroutine package for calculation of seismic normal-mode solution, *Seismological Algorithm*.

Searle, M., Noble, S., Cottle, J., Waters, D., Mitchell, A., Hlaing, T., & Horstwood, M. (2007). Tectonic evolution of the Mogok metamorphic belt, Burma (Myanmar) constrained by U-Th-Pb dating of metamorphic and magmatic rocks. *Tectonics*, *26*, TC3014. https://doi.org/10.1029/2006TC002083

Searle, M. P., Morley, C. K., Waters, D. J., Gardiner, N. J., Htun, U. K., Than Than, N., & Robb, L. J. (2017). Chapter 12: Tectonic and metamorphic evolution of the Mogok Metamorphic and Jade Mines belts and ophiolitic terranes of Burma (Myanmar). *Geological Society, London, Memoirs*, *48*(1), 261–293. https://doi.org/10.1144/m48.12

Shen, W., & Ritzwoller, M. H. (2016). Crustal and uppermost mantle structure beneath the United States. *Journal of Geophysical Research: Solid Earth*, *121*, 4306–4342. https://doi.org/10.1002/2016JB012887

Shen, W., Ritzwoller, M. H., Schulte-Pelkum, V., & Lin, F.-C. (2012). Joint inversion of surface wave dispersion and receiver functions: A Bayesian Monte-Carlo approach. *Geophysical Journal International*, *192*(2), 807–836.

Singh, A., Bhushan, K., Singh, C., Steckler, M. S., Akhter, S. H., Seeber, L., et al. (2016). Crustal structure and tectonics of Bangladesh: New constraints from inversion of receiver functions. *Tectonophysics*, *680*, 99–112. https://doi.org/10.1016/j.tecto.2016.04.046

Sloan, R. A., Elliott, J. R., Searle, M. P., & Morley, C. K. (2017). Chapter 2: Active tectonics of Myanmar and the Andaman Sea. *Geological Society, London, Memoirs*, *48*(1), 19–52. https://doi.org/10.1144/m48.2

Socquet, A., Vigny, C., Chamot-Rooke, N., Simons, W., Rangin, C., & Ambrosius, B. (2006). India and Sunda plates motion and deformation along their boundary in Myanmar determined by GPS. *Journal of Geophysical Research*, *111*, B05406. https://doi.org/10.1029/2005JB003877

Steckler, M. S., Mondal, D. R., Akhter, S. H., Seeber, L., Feng, L., Gale, J., et al. (2016). Locked and loading megathrust linked to active subduction beneath the Indo-Burman Ranges. *Nature Geoscience*, 9(8), 615–618. https://doi.org/10.1038/ngeo2760

Stork, A., Selby, N., Heyburn, R., & Searle, M. (2008). Accurate relative earthquake hypocenters reveal structure of the Burma subduction zone. *Bulletin of the Seismological Society of America*, 98(6), 2815–2827. https://doi.org/10.1785/0120080088

Tanimoto, T., & Rivera, L. (2008). The ZH ratio method for long-period seismic data: Sensitivity kernels and observational techniques. *Geophysical Journal International*, 172(1), 187–198. https://doi.org/10.1111/j.1365-246X.2007.03609.x

Thiam, H. N., Htwe, Y. M. M., Kyaw, T. L., Tun, P. P., Min, Z., Htwe, S. H., et al. (2017). A report on upgraded seismic monitoring stations in Myanmar: Station performance and site response. *Seismological Research Letters*, 88(3), 926–934. https://doi.org/10.1785/0220160168

Vigny, C., Socquet, A., Rangin, C., Chamot-Rooke, N., Pubellier, M., Bouin, M. N., et al. (2003). Present-day crustal deformation around Sagaing fault, Myanmar. *Journal of Geophysical Research*, 108(B11), 2533. https://doi.org/10.1029/2002JB001999

Wang, X., Chen, Q. F., Li, J., & Wei, S. J. (2016). Seismic sensor misorientation measurement using P-wave particle motion: An application to the NECsaids array. *Seismological Research Letters*, 87(4), 901–911. https://doi.org/10.1785/0220160005

Wang, X., Wei, S., & Wu, W. (2017). Double-ramp on the Main Himalayan Thrust revealed by broadband waveform modeling of the 2015 Gorkha earthquake sequence. *Earth and Planetary Science Letters*, 473, 83–93. https://doi.org/10.1016/j.epsl.2017.05.032

Wang, Y., Sieh, K., Aung, T., Min, S., Khaing, S. N., & Tun, S. T. (2011). Earthquakes and slip rate of the southern Sagaing fault: Insights from an offset ancient fort wall, lower Burma (Myanmar). *Geophysical Journal International*, 185(1), 49–64. https://doi.org/10.1111/j.1365-246X.2010.04918.x

Wang, Y., Sieh, K., Tun, S. T., Lai, K.-Y., & Myint, T. (2014). Active tectonics and earthquake potential of the Myanmar region. *Journal of Geophysical Research: Solid Earth*, 119, 3767–3822. https://doi.org/10.1002/2013JB010762

Wessel, P., Smith, W. H., Scharroo, R., Luis, J., & Wobbe, F. (2013). Generic mapping tools: Improved version released. *Eos, Transactions American Geophysical Union*, 94(45), 409–410. https://doi.org/10.1002/2013EO450001

Xiong, X., Shan, B., Zhou, Y., Wei, S., Li, Y., Wang, R., & Zheng, Y. (2017). Coulomb stress transfer and accumulation on the Sagaing fault, Myanmar over the past 110 years and its implications for seismic hazard. *Geophysical Research Letters*, 44, 4781–4789. https://doi.org/10.1002/2017GL072770

Yao, H., Van Der Hilst, R. D., & Montagner, J. P. (2010). Heterogeneity and anisotropy of the lithosphere of SE Tibet from surface wave array tomography. *Journal of Geophysical Research*, 115, B12307. https://doi.org/10.1029/2009JB007142

Yeck, W. L., Sheehan, A. F., & Schulte-Pelkum, V. (2013). Sequential H-κ stacking to obtain accurate crustal thicknesses beneath sedimentary basins. *Bulletin of the Seismological Society of America*, 103(3), 2142–2150. https://doi.org/10.1785/0120120290

Zhu, L. P. (2000). Crustal structure across the San Andreas Fault, southern California from teleseismic converted waves. *Earth and Planetary Science Letters*, 179(1), 183–190. https://doi.org/10.1016/s0012-821x(00)00101-1

Zhu, L. P., & Helmberger, D. V. (1996). Advancement in source estimation techniques using broadband regional seismograms. *Bulletin of the Seismological Society of America*, 86(5), 1634–1641.

Zhu, L. P., & Rivera, L. A. (2002). A note on the dynamic and static displacements from a point source in multilayered media. *Geophysical Journal International*, 148(3), 619–627. https://doi.org/10.1046/j.1365-246X.2002.01610.x